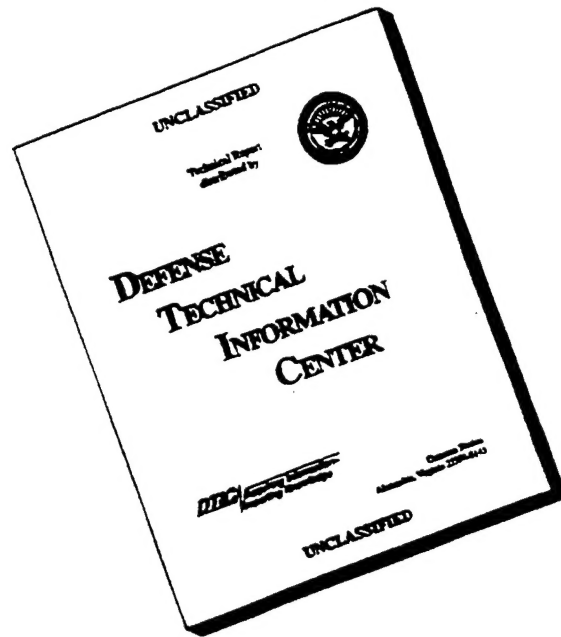
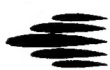


REPORT DOCUMENTATION PAGE			Form Approved OMB No. 0704-0188
Public reporting burden for this collection of information is estimated to average 1 hour per response, including the time for reviewing instructions, searching existing data sources, gathering and maintaining the data needed, and completing and reviewing the collection of information. Send comments regarding this burden estimate or any other aspect of this collection of information, including suggestions for reducing this burden to Washington Headquarters Services, Directorate for Information Operations and Reports, 1215 Jefferson Davis Highway, Suite 1204, Arlington, VA 22202-4302, and to the Office of Management and Budget, Paperwork Reduction Project (0704-0188), Washington, DC 20503.			
1. AGENCY USE ONLY (Leave blank)	2. REPORT DATE  1994	3. REPORT TYPE AND DATES COVERED  Final Report	
4. TITLE AND SUBTITLE  Investigation of Relaxation Processes in Flow About Models in Hypersonic Wind Tunnels of Different Types		5. FUNDING NUMBERS  F6170893W0695	
6. AUTHOR(S)  Professor Vadim Alfeyorov			
7. PERFORMING ORGANIZATION NAME(S) AND ADDRESS(ES)  Central Aerodynamics Institute (TsAGI) 140160 Zhukovsky Moscow Russia		8. PERFORMING ORGANIZATION REPORT NUMBER  SPC-93-4044	
9. SPONSORING/MONITORING AGENCY NAME(S) AND ADDRESS(ES)  EOARD PSC 802 BOX 14 FPO 09499-0200		10. SPONSORING/MONITORING AGENCY REPORT NUMBER  SPC-93-4044	
11. SUPPLEMENTARY NOTES  <b>DTIC QUALITY INSPECTED</b>			
12a. DISTRIBUTION/AVAILABILITY STATEMENT  Approved for public release; distribution is unlimited.		12b. DISTRIBUTION CODE  A	
13. ABSTRACT (Maximum 200 words)  This report presents the theoretical and experimental results related to flows over such simple bodies as semisphere, cone, and wedge. These were investigated in hypersonic wind tunnels of various classes at nearly equal Mach and Reynolds numbers (M from 7.0 to 8.0, Re <sub>0</sub> from 135 to 240) but at notably differing free-stream velocities: 790, 2700 and 6000 m/s. Hypersonic resistance- and arc-heating wind tunnels and a hypersonic MHD-accelerator wind tunnel, as well as their test equipment are described. A technique to determine parameters of a free stream over a model including gasdynamic ones (M, Re, Re <sub>0</sub> , T, P, V, H <sub>0</sub> , H) and physico-chemical ones (γ, T <sub>0</sub> , T <sub>v</sub> , T <sub>n</sub> , C <sub>f</sub> ), as well as a verification procedure are presented. Experimental data on pressure distribution over models, shock wave positions/shapes were obtained. The experimental data are compared with respective calculated results obtained by using the VSL theory and the Navier-Stokes equations for the test conditions adopted. Interrelation of the theoretical and test data is shown not to be unambiguous, especially in what concerns locations and shapes of shock waves. The VSL theory is employed to compute local parameters of the shock layer. The influence of alkali metal seed on the rate of relaxation in the shock-layer is considered. Features of profiles of both temperature and air component concentrations in the shock layer are shown to be useful in explaining a set of phenomena revealed in experiments: a radiation offset upstream of a sphere hypervelocity shock layer, a radiation relaxation at a cone apex. The impact of the seed metal is shown to be insignificant.			
14. SUBJECT TERMS		15. NUMBER OF PAGES  70	
		16. PRICE CODE	
17. SECURITY CLASSIFICATION OF REPORT  UNCLASSIFIED	18. SECURITY CLASSIFICATION OF THIS PAGE  UNCLASSIFIED	19. SECURITY CLASSIFICATION OF ABSTRACT  UNCLASSIFIED	20. LIMITATION OF ABSTRACT  UL

# DISCLAIMER NOTICE



**THIS DOCUMENT IS BEST  
QUALITY AVAILABLE. THE  
COPY FURNISHED TO DTIC  
CONTAINED A SIGNIFICANT  
NUMBER OF PAGES WHICH DO  
NOT REPRODUCE LEGIBLY.**



**INVESTIGATION OF RELAXATION  
PROCESSES IN FLOW ABOUT MODELS IN  
HYPERSONIC WIND TUNNELS OF  
DIFFERENT TYPES**

**FINAL REPORT UNDER CONTRACT CPS-93-4044**

**Study supervisor**

Prof. V.I. Alfyorov

**Study team:**

V.I. Alfyorov

A.S. Bushmin

G.I. Shcherbakov

L.M. Dmitriyev

A.P. Rudakova

B.V. Yegorov

I.V. Yegorov

Yu.Ye. Markachev

V.N. Skirda

A.N. Morozov

A.A. Orlov

**Zhukovsky  
1994**

19970506 089

### ABSTRACT

This report presents the theoretical and experimental results related to flows over such simple bodies as semishpere, cone, and wedge. These were investigated in hypersonic wind tunnels of various classes at nearly equal Mach and Reynolds numbers ( $M$  from 7.0 to 8.0,  $Re_0$  from 135 to 240) but at notably differing free-stream velocities: 790, 2700 and 6000 m/s.

Hypersonic resistance- and arc-heating wind tunnels and a hypersonic MHD-accelerator wind tunnel, as well as their test equipment are described. A technique to determine parameters of a free stream over a model including gasdynamic ones ( $M$ ,  $Re$ ,  $Re_0$ ,  $T$ ,  $P$ ,  $V$ ,  $H_0$ ,  $H$ ) and physico-chemical ones ( $\gamma$ ,  $T_0$ ,  $T_V$ ,  $T_n$ ,  $C_i$ ), as well as a verification procedure are presented.

Experimental data on pressure distribution over models, shock wave positions/shapes were obtained. The experimental data are compared with respective calculated results obtained by using the VSL theory and the Navier-Stokes equations for the test conditions adopted. Interrelation of the theoretical and test data is shown not to be unambiguous, especially in what concerns locations and shapes of shock waves.

The VSL theory is employed to compute local parameters of the shock layer. The influence of alkali metal seed on the rate of relaxation in the shock-layer is considered. Features of profiles of both temperature and air component concentrations in the shock layer are shown to be useful in explaining a set of phenomena revealed in experiments: a radiation offset upstream of a sphere hypervelocity shock layer, a radiation relaxation at a cone apex. The impact of the seed metal is shown to be insignificant.



## INTRODUCTION

The development of a new generation of hypersonic transatmospheric vehicles featuring high L/D-ratios such as NASP requires that the physico-chemical processes inherent in flows over vehicles be studied more comprehensively, on the one hand, and such test facilities be constructed which are capable of reproducing these processes adequately, on the other hand.

The ranges of speeds and pressures for which these studies should be carried on are governed by flight paths of such vehicles. Their acceleration to orbital velocities occurs in relatively dense atmosphere; they can also perform maneuvers at altitudes of 50 km to 70 km and at flight speeds of  $M=20$  to  $M=25$ .

Many known articles are devoted to the description of flow fields of chemically reacting gases both over simple bodies and real vehicles [1], [2], [3].

The thermochemical models underlying these calculations and the numerical algorithms developed by different authors differ considerably because of a number of unverified assumptions.

In the calculations, the differences in reaction rate constants for flows in thermodynamic equilibrium are not as important as nonequilibrium ones. In non-equilibrium, the flow field depends greatly on the thermochemical model used by the authors. In most previous investigations, the reaction rate is supposed to depend on translational temperature only. In latest publications [4], [5], the chemical reaction rate is assumed to depend both on translational and vibrational temperatures because of a close relationship of dissociation with vibrational degrees of freedom. The temperatures of rotational and electron-vibrational degrees of freedom are also assumed to be different. Considerable gradients in concentrations of different air components and excited electron states occur under the flow conditions behind the shock wave front. The tests carried out in shock wind tunnels [6] show the concentration of NO to vary most rapidly behind the shock wave, with this concentration starting to rise immediately following the oxygen dissociation. A rapid NO electronic excitation behind the shock wave, owing to the high translational temperature, leads to an intensive ultraviolet emission in the Gamma band system ( $\lambda=200$  to  $320$  nm).

The situation is further complicated by nonequilibrium emission caused also by other air components both in visual and ultraviolet and infrared regions. The intensity of nonequilibrium emission can exceed that of equilibrium emission by a factor of 2 to 15 [7]. However, these calculations [8] are not confirmed by flight test results, although the intensity of radiation heating exceeds convective heating intensity.

All these considerations dictate that the thermochemical models and mathematical algorithms be verified in laboratory conditions. It is desirable to choose those speed and pressure conditions which could allow comparison of the results obtained by different authors in various facilities and of respective numerical algorithms.

The simplest technique to reproduce the conditions of hypersonic equilibrium flows over bodies is the application of gases having specific-heat ratios of  $\gamma=1.2$  to  $1.18$  such as Freon-14 ( $\text{CF}_4$ ) [9]. In this case, it is possible to reproduce shock stand-off distance which is an integral parameter characterizing the sink of kinetic energy into internal degrees of freedom. In [10], hypersonic flows with

different properties of the test gas (Freon-14 ( $\gamma=1.18$ ), air ( $\gamma=1.4$ ), helium ( $\gamma=1.67$ )) over conical bodies are investigated experimentally. These tests yielded some distributions of surface pressures, shock wave stand-off distances and shock shapes. It is inferred from these data that the real gas effects at high cone angles result in an appreciable difference in trim angles of attack and L/D-ratios as compared to respective results obtained in test facilities using air as a test gas. A review of various types of aerodynamic facilities capable of reproducing real gas effects and techniques for their investigation is given in [11] which also contains a description of their merits and weaknesses.

The authors believe that such facilities are, first of all, shock tunnels, conventional shock wind tunnels and shock wind tunnels without shock wave reflection. Various experiments carried out in them have been considered. Among these, optical methods are pointed out as enabling the determination of shock stand-off distances and shapes, as well as ranges of their possible application depending on gas density.

Special consideration is given to the capabilities of holographic flow visualization techniques. It is suggested that emission spectra of the first negative system of nitrogen  $N_2$  be applied to determine its vibrational temperature level. The authors maintain that the CARS technique used to determine  $T_{rot}$ ,  $T$ , main molecule states of  $N_2$ ,  $O_2$ ,  $NO$ , etc. is the most promising one for the study of the kinetics of physico-chemical processes past shock waves. This technique is, however, rather expensive and labor-intensive.

An important feature characterizing relaxation processes of flows over bodies is pressure distributions on the body surfaces [12] which are dependent on shock shapes.

Another type of test facilities capable of producing full-scale flow velocities of  $V=6$  to  $8$  km/s is ballistic range facilities equipped with light-gas guns. Thus, a test program has been carried out at the AEDC Research Center aimed at investigating flows over various models fired by  $6.35$  mm guns at velocities of up to  $8$  km/s both in air and pure nitrogen. In these tests, shock positions and shapes, coefficients of normal forces and pitch moments, as well as locations of the centers of pressure were recorded [13].

As in [14], the thermodynamic gas state influences the boundary layer stability considerably which, in turn, appreciably alters its sensitivity to different disturbing frequencies and thereby the transition Reynolds numbers redistributing heat fluxes on body surface.

Theoretical and experimental data on shock shapes and stand-off distances for a sphere, a wedge, a cone, a cylinder and models of hypersonic vehicles AOTV, PAET are compared in [15] for the range of velocities of  $4$  to  $8$  km/s and pressures of  $2 \cdot 10$  to  $10^4$  Pa. All the experimental data are obtained in shock wind tunnels and ballistic range facilities. The comparison is given for different thermodynamic gas models. It is concluded that the six-temperature model with seven chemical air components is in better agreement with experimental data than the one-temperature model. The model of a perfect gas and a thermodynamic equilibrium gas is inadequate for the cases under discussion. Unfortunately, the test model material used is not specified. Depending on the level of model surface catalicity, the shock stand-off distance may vary under such conditions by  $10\%$  to  $18\%$  [16].

Short run times in shock wind tunnels and small dimensions of models in ballistic test rigs restrict the capabilities of experimental investigations of nonequilibrium processes considerably.

The application of classical wind tunnels for these purposes is impeded because of technical and physical reasons.

It is shown in [17] that in order to reproduce hypersonic flight conditions in a wind tunnel test section, three conditions must be satisfied simultaneously:

$$\frac{u^2}{2} \geq H; \quad \frac{u^2}{2} \geq E_{\text{dis}} + E_v;$$

$$\frac{\tau_{\text{chem.m}}}{\tau_{\text{aerod.m}}} \approx \frac{\tau_{\text{chem.n}}}{\tau_{\text{aerod.n}}}.$$

As for classical wind tunnels, they prove to be incapable of realizing in full either the first or the second condition. Even if it could be possible to overcome technical problems of achieving and maintaining the plenum chamber gas parameters required to obtain a test section flow with full-scale velocities, i.e.  $u > 3$  to  $4$  km/s, the study of nonequilibrium processes would be impossible. When the dissociated gas is expanded in a hypersonic nozzle, a considerable portion of stagnation enthalpy becomes "frozen" in internal degrees of freedom and chemical reactions. The part of "frozen" energy can amount to 50% and more. The specific heat ratio is also "frozen", and the flow over a body becomes equivalent to an ideal gas flow.

A hypersonic MHD-air flow acceleration wind tunnel constructed and operated at TsAGI is capable of satisfying the above-stated requirements. It is possible to achieve a flow of  $4$  to  $8$  km/s in its test section at  $M=5$  to  $15$  [18, 19] which enables comparative studies of identical models tested in hypersonic wind tunnels of different types with close similarity parameters, sufficiently similar Mach and Reynolds numbers, but with significantly different effects of physical and chemical processes influencing the flow. For this reason, TsAGI's hypersonic MHD-acceleration wind tunnel is a desirable platform for comparative testing of results from other facilities featuring perfect gases, gases with excited vibrational states and low dissociation levels. As shown in [20], such an approach has proven to be rather effective in the research of gas dynamics and heat transfer to scramjet combustion chamber components.

It is also advisable to apply models of simple shapes (hemisphere, wedge, cone) for comparative tests so as to identify real gas effects for which a theoretical analysis is simple and for which there are test results obtained by other investigators.

It is important to deal with those velocities and initial pressures which have been already studied in previous tests in shock wind tunnels when nonequilibrium effects were governing. According to [6] and [11], the flow velocities required should be from  $6$  km/s to  $8$  km/s and flow pressures from  $40$  Pa to  $400$  Pa. These parameters are also characteristic of an intensive nonequilibrium radiation from shock layer.

This investigation conducted under contract SPC-93-4044 deals with comparative tests aimed at establishing real gas effects on flows over simple bodies in test facilities of different types.

## DESCRIPTION OF WIND TUNNELS, INSTRUMENTATION AND MODELS

Ohmic (resistor-type) heating wind tunnels have found a wide application in the investigations of hypersonic perfect-gas flows. The arc-heating facilities are capable of producing flows of both vibrationally-excited gases and weakly-dissociated ones. Tests were conducted at stagnation temperatures of 400 K to 1000 K and 2500 K to 4000 K and flow velocities of 800 m/s to 1200 m/s and 2500 m/s to 3000 m/s, respectively.

A hypervelocity MHD-gas acceleration wind tunnel makes it possible to achieve flow velocities of  $4 \cdot 10^3$  to  $8 \cdot 10^3$  m/s. Since the values viscosity of  $\mu_0$  are rather great because of a high stagnation enthalpy past a shock wave near a test model, the Reynolds numbers,  $Re_0$ , will be relatively moderate. Therefore, the Reynolds numbers,  $Re_0$ , realized in this wind tunnel is considered to be a basis from which to choose other wind tunnels and their operation regimes.

The Reynolds numbers,  $Re_0$ , attained in hypersonic TsAGI wind tunnels with ohmic gas heating are considerably higher than those achieved in the hypervelocity wind tunnel. Therefore, their direct employment without undertaking additional examination efforts which are beyond the scope of financing the present study seems to be impossible.

In view of the above considerations, the hypersonic low-density wind tunnel VAT-102 has been chosen to reproduce this velocity range [21]. The maximum Mach number  $M=8$  realized in this wind tunnel serves as a criterion for choosing Mach numbers required for the present investigations.

For the second temperature and velocity range realized, the arc-gas heater test facility of the MHD test rig of TsAGI was applied which is capable of producing both nonequilibrium and equilibrium flows with high-stability parameters.

Comparison of wind tunnel characteristics in terms of the level of their test section blockage shows that axisymmetric models with midsection diameter of  $d_m=0.04$  m can be used in all three cases. Then the standard operation Reynolds number based on the parameters past a shock wave for the wind tunnel VAT-102 will be  $Re_0 \sim 200$ .

All the above considerations dictated the choice of the dimensions for the main components and operation regimes of the wind tunnels selected; their brief characteristics are given below.

The low-density wind tunnel VAT-102 is a low-temperature ( $T_0=300$  K to 400 K) vacuum facility designed for testing models within the ranges of  $Re=50$  to 1000 and  $M=5$  to 8 (Fig.1). Pure nitrogen used as a test gas is supplied from bottles passing through an ohmic heater to plenum chamber 1 equipped with honeycomb 2 and then it flows on the model through a supersonic contoured axisymmetric nozzle 3. The test section is designed as an Eiffel chamber connected via a gate to a vacuum vessel of about  $150 \text{ m}^3$ . The vacuum vessel pressure is maintained by vapor oil booster pumps of a total capacity of  $10^2 \text{ m}^3/\text{s}$  at  $P=2$  Pa used as the first stage. Two-rotor pumps 2DBH-1500 connected to mechanical pumps HB3-500 are installed at their exit.

The given tests were conducted using a contoured nozzle with the throat size of  $\sim 7.5 \cdot 10^{-3}$  m and the exit diameter of 0.185 m, the flow core diameter being 0.065 m. The measurements included plenum chamber gas pressures and

temperatures as well as flow fields past shock waves  $P'_0$ , at nozzle exit and along nozzle axis. The results obtained are given in Figs. 2 and 3. According to these measurements, the Mach number  $M=7.63$  at  $P_{st}=2$  Pa and respective model Reynolds numbers  $Re_0=270$  to  $300$ ,  $Re_\infty \approx 3800$  to  $4000$  were achieved in the test section, that is, the values were close to predicted ones. The measurement error was  $\pm 3\%$  for pressures and  $\sim 1\%$  for mean-mass temperatures.

Static test section flow temperatures were  $\sim 23$  to  $27$  K which meant that they were lower than those of the curve of nitrogen equilibrium condensation values. But because of the nonequilibrium condensation effect featuring this static pressure, it was decided to confine the plenum chamber gas temperature to  $340$  K.

Figure 4 taken from [22] compares the conditions realized in this experiment with the region of nonequilibrium condensation. It is seen that there was no nitrogen condensation.

The application of shadow, direct shadow and interferometric visualization techniques proved to be impossible because of a low gas density in the test section. Therefore, the flows over bodies were visualized by applying a version of the glow discharge method. Narrow electrodes ( $d \sim 1$  cm) were placed outside the flow, parallel to each other in the place of the model position. In order to exclude break-downs, the side walls were insulated. The controlled voltage of about  $2.5$  kV was applied to the electrodes, the current was  $\sim 50$   $\mu$ A. The electrons accelerated in the cathode layer collided with nitrogen molecules causing them to glow. Glow intensity was proportional to flow density. Glow video recordings and direct photographs were made.

The circuit of the wind tunnel with air flow arc-heating is shown in Fig. 5. The wind tunnel consists of the following main components: an arc heater, a supersonic nozzle, a test section in the form of an Eiffel chamber with windows to observe models and a device for a rapid model introduction into flow. The gas exhaust system includes a supersonic diffuser and a subsonic diffuser, a cooling system and a four-stage ejector system to provide for a total compression ratio of about 120.

The arc heater has a coaxial design with an arc rotated by magnetic field. The special magnetic field shape and the design of heater components make it possible to minimize high-frequency discharge current and voltage fluctuations and exclude almost completely low-frequency fluctuations thereby ensuring a high stability of parameters of heated gases. A detailed description of the heater and the structure of electric discharge occurring in it is given in [23,24].

It is possible to add alkali seeds to the heater flow which enables various optical investigations and, besides, makes it possible to have an almost equilibrium flow.

A conical nozzle with a square  $150 \times 150$  mm<sup>2</sup> exit section was used in these tests. In a number of other tests, a nozzle based on the secondary MHD-accelerator nozzle was applied.

The measurement system designed for this wind tunnel allowed recording of gas and alkali seed flow rates, pressures, heater currents and voltages, distributions of static pressures along the nozzle and static pressures in the Eiffel chamber, as well as pressure fields past a normal shock wave  $P'_0$  and at nozzle exit. Magneto-inductance gages were used to measure pressures within required ranges with the data recorded by a computer. The wind tunnel was run as follows. After the wind tunnel was started and the required test regime stabilized, the model was

introduced into the flow. After some 5 to 7 s the model was removed from the test section and the wind tunnel switched off.

In some tests, alkali seeds were injected into the flow; this was done when, as a rule, the model was already in the flow.

The parameters that were impossible to measure at the nozzle exit were determined using known gas dynamic relations for an equilibrium, frozen gas flow with  $\gamma = 1.4$  and for a flow with instantaneously frozen parameters at different section positions. These sections were chosen based on measured static nozzle pressure distributions, pressure values  $P_0'$  and pressure fields. Typical flow parameters at nozzle exit for the present tests are given in Fig. 6.

The hypervelocity MHD-air acceleration wind tunnel is a unique test facility. Its detailed description is given in [25]. Fig. 7 presents the circuit of the wind tunnel and Figs. 8 and 9 its general views.

The operation of the wind tunnel was conducted as follows. A gas heated in heater (1) up to  $T_0 \sim 3500$  K at  $P_0$  of about  $2 \cdot 10^5$  Pa was supplied to mixing chamber (2) where slightly ionized seeds (1% of weight) were injected by metering device (3). Then the gas passing through primary supersonic nozzle (4) entered MHD-accelerator (5) where it accelerated in cross constant electric and magnetic fields up to required velocities. After the gas was expanded to specified static parameters in secondary nozzle (6), it was introduced into the test section (7) with a model inside and exhausted to the atmosphere through a diffuser, a cooling device and a set of ejectors.

The arc heater features a coaxial design having an arc rotated by magnetic field; it is similar to that used in the above described hypersonic wind tunnel.

The supply of seeds in the form of KNa eutectics to the mixing chamber serving as the wind tunnel plenum chamber was accomplished by a metering device that was a combination of a plunger press and a displacement supply system whose supply lines were protected by an inert gas [26]. Optimal placement and a special injector ensured finely-ground seeds ( $d_d \sim 5$  mk) and their uniform distribution across flow section. As a result, a supersonic current conducting flow was formed that featured required conductivity and rather high stability of its parameters [27].

A primary supersonic nozzle designed for  $M=2$  was installed between the mixing chamber and the MHD-accelerator. Its outlet parameters were matched with the inlet parameters of the MHD-accelerator channel.

The MHD-accelerator consists of two main units: an accelerating chamber (MHD-channel) and an electromagnet. The Faraday-type rectangular MHD-channel includes two sectionalized electrode walls and two isolating walls perpendicular to them. The magnetic field with induction of up to  $B=2.5$  T is produced by an electromagnet composed of two E-shaped parts with an MHD-channel between its bars. It is possible to apply MHD-channels of different lengths and sections when the magnetic system dimensions are also varied as required. A detailed description of accelerator design features is given in [28].

These tests used a MHD-channel 555 mm in length, an input section of  $15 \times 15$  mm<sup>2</sup>, an output section of  $15 \times 25$  mm<sup>2</sup> with 60 electrode pairs, and electrode sectioning in steps of  $S=8$  mm. A magnetic field with induction of  $B=2.37$  T was produced along a length of 435 mm, and the uniform magnetic field extended for about 390 mm. The operating (energized) electrodes were placed within the uniform magnetic field. Thirty five pairs of operating electrodes were used.



The accelerator power supply system was based on three-phase transformers containing 1 to 20 isolated secondary three-phase windings. Each winding was connected to the respective electrode pair through a three-phase bridge-circuit rectifier, a ballast resistance and a smoothing choke. Thyristor voltage regulators were applied at transformer inlets. This kind of power supply made it possible to have 120 independent electrode power units with no-load voltage from 580 V to 1300 V and current of up to 100 A. The voltage fluctuations due to active loads did not exceed 1%.

Three transformers with 15, 10 and 10 power circuits and voltages of 600 V, 900 V and 900 V, respectively, were used in the present tests.

Removable secondary rectangular nozzles were attached to the MHD-accelerator channel through an insulating spacer. The nozzle inlet was matched with the channel outlet. A special nozzle with an exit section of  $111 \times 111 \text{ mm}^2$  was designed and manufactured for these tests, the upper and lower wall angles being  $6^\circ$  and side wall angle  $6^\circ 30'$ .

The test section was designed in the form of the Eiffel chamber and equipped with windows for visual observations, filming and photographing, as well as with a device for introducing models into flow. The exhaust system was similar to that used in the hypersonic wind tunnel with an arc gas heater.

The wind tunnel was started as follows. When the heater attained the steady-state regime, seeds were added and the model was introduced into flow after which the voltage was being applied to the accelerator electrodes during  $0.5 \div 2 \text{ s}$  with simultaneous photographing and optical measurements. After the accelerator was deenergized and the model was removed from flow, the seed supply was stopped and the heater was switched off. The electromagnet and recording devices were switched on before the heater discharger was initiated.

The measurement system made it possible to measure the following parameters: gas and seed flow rates, pressure, current and voltage in heater, current in electromagnet, static pressure distributions along MHD-channel and secondary nozzle, current and voltage distributions on electrodes along MHD-channel length, static pressure and pressure field past a normal shock  $P_0'$  in test section. The pressure was measured by using magneto-inductance pressure transducers of different measurement ranges, the current and voltage by shunts and voltage dividers.

During the preparation for the present tests, the recording operation of the parameters being measured by previously used oscillographs was switched over to a computer which necessitated considerable updating of the measuring circuits to provide for a more reliable insulation of pressure transducers from wind tunnel components and the application of complicated galvanic isolation systems in the circuits used to measure electric quantities. The measurement error for pressure was no more than 3% and that for electric quantities was no more than 2%.

The evaluation of flow parameters in the test section of an MHD-gas acceleration facility is a more complicated process than in conventional wind tunnels, since stagnation parameters vary continuously along the channel under the action of ponderomotor forces and Joule dissipation. Direct measurements of gasdynamic parameters in a high-energy flow present considerable difficulties. To facilitate their determination, a procedure [29] based on a numerical solution of the so-called "inverse" flow problem was utilized. This procedure is effective when measured parameters and dependences are applied as boundary and initial conditions and lack solutions from a set of gas flow equations.

The MHD-channel flow parameters not subject to measurement were calculated in a thermodynamic equilibrium assumption by numerical solution of a set of quasidimensional equations of magnetic gas dynamics reduced to the following form:

$$\begin{aligned} \rho u \frac{du}{dx} &= -\frac{dP}{dx} + j_y B - 2C_f \frac{\rho u^2}{D}; \\ \rho u^2 \frac{du}{dx} + \rho u \frac{dH}{dx} &= j_y E_y^* + j_x E_x - Q_w; \\ \rho U F &= \dot{m}; \quad H = H(P, T); \\ j_y(x) &= \frac{I_e(x)}{S_b}; \quad E_y^*(x) = \frac{V_e(x) - \Delta V_{near}}{h_{heom.}(x)}; \\ j_x &= \frac{r-1}{r\beta_H} j_y; \quad E_x = \frac{r(1+\beta_H^2) - 1}{r\delta\beta_H} j_y; \\ r &= \left(1 + \frac{S}{h}\beta_H\right)^{-1}. \end{aligned}$$

Geometric channel parameters, measured pressure distributions, magnetic induction, and current and voltage along the channel length were introduced into the equations. Flow parameters measured at accelerator channel input were used as initial conditions.

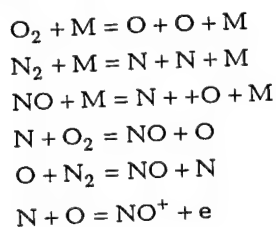
Thermodynamic functions, transfer coefficients and electric conductivity  $\delta$  (equilibrium) were calculated by using standardized programs [31, 32];  $C_f$  was determined by the procedure in [33],  $Q_w$  and  $\Delta V_{near}$  were taken from [34].

The reliability of the calculated data obtained by the above technique was verified by the agreement of calculated flow velocities in the accelerator channel and determined using measured values of induced potential difference  $V = uBh$  on a test electrode pair placed downstream of the energized zone.

Measured and calculated parameter distributions along the channel length typical for the given test series are given in Fig.10. Their variations from run to run do not exceed 3 to 5%.

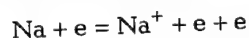
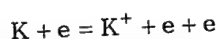
Gasdynamic parameters and thermodynamic gas functions in the test section and their distributions in the secondary nozzle were calculated taking account of nonequilibrium effects for static pressure nozzle distributions obtained experimentally.

Quasidimensional equations of gas dynamics were solved numerically together with equations of kinetics. It was assumed that the following chemical and ionization reactions proceed in air in the test ranges of temperatures and pressures:





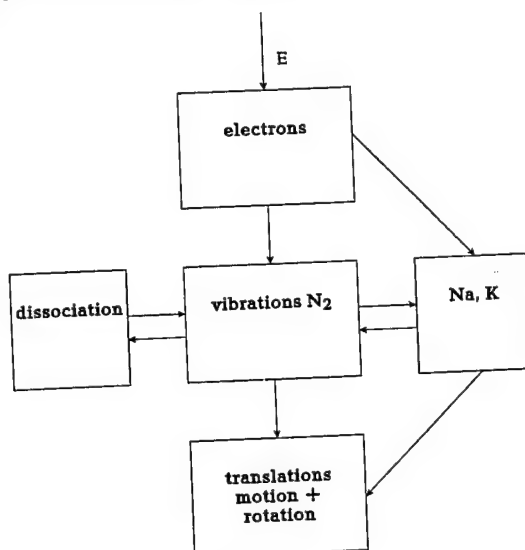
These reactions were accomplished by ionization reactions between K and Na seeds:



Here M is any particle of  $O_2$ ,  $N_2$ ,  $NO$ ,  $O$ ,  $N$ ,  $NO^+$ ,  $K$ . The equations were integrated by the method of Gear. The correlation of calculated parameters to test conditions was checked by the agreement of calculated and measured values of the static pressure and the pressure behind a normal shock at the secondary nozzle exit. Fig. 11 shows typical flow parameters in the secondary nozzle and at its exit.

In order to evaluate possible influence of nonequilibrium processes in a gas accelerated in the MHD-channel they were included, under the present grant, into the following thermodynamic model.

The scheme of energy transfer from the electric field E to internal gas degrees of freedom used in the calculations is as follows:



The equation for full enthalpy H is:

$$\frac{d}{dx} (\rho H_0 u F) = \frac{V_k I_k}{S} \beta, \quad (1)$$

where coefficient  $\beta$  represents complete energy losses (including energy losses for radiation, electrode losses and heat fluxes to walls).

The equation for energy flux inherent in  $N_2$  molecule vibrations has the form:

$$\frac{d}{dx} \left( \frac{E_{V_1}}{m_1} \rho_1 u F \right) = \beta_1 \frac{(V_k \beta - u B h_k)}{S} I_k + (Z_{1VT} + Z_{1VV'} + Z_{1chem}) \cdot F \quad (2)$$

Parameter  $\beta_1$  is the ratio of energy transferred to the vibrational degree of freedom of  $N_2$  to the total energy transferred from electrons to internal gas degrees of freedom.

Rates  $Z_1$  of energy transfer to vibrations in the processes VT, VV' and in chemical reactions are calculated by using relations given in [35 to 39].

The equations for  $O_2$  and NO molecule vibrations have the similar form:

$$\frac{1}{F} \frac{d}{dx} \left( \frac{E_{V_2}}{m_2} \rho_2 u F \right) = Z_{2VT} + Z_{2VV'} + Z_{2chem} \quad (3)$$

$$\frac{1}{F} \frac{d}{dx} \left( \frac{E_{V_3}}{m_3} \rho_3 u F \right) = Z_{3VT} + Z_{3VV'} + Z_{3chem} \quad (4)$$

The gas composition is determined, accounting for the following reactions:



The equations for particle flows are written as follows:

$$\frac{1}{F} \frac{d}{dx} \left( \frac{\rho_i}{m_i} u F \right) = J_i \quad (i = 1, 6) \quad (6)$$

Chemical reaction rate constants (6) required to calculate functions of particle collision  $J_i$  are taken from [35 to 37].

The total enthalpy  $H_0$  is derived from relations from [35 to 37]:

$$\begin{aligned} H_0 &= \frac{u^2}{2} + H \\ H &= \sum_{i=1}^6 \frac{\rho_i}{\rho} H_i \\ H_i &= RT \frac{\pi_i}{m_i} + \frac{E_{V_i}}{m_i} + \epsilon_i \\ \pi_i &= \frac{7}{2} \quad \text{for } i = 1, 3; \quad \pi_i = \frac{5}{2} \quad \text{for } i = 4, 6 \end{aligned} \quad (7)$$

The equations for momentum flow are used in the form:

$$\frac{d}{dx} \left[ (P + \rho u^2) F \right] = -2C_f \frac{\rho u^2 F}{D} + \frac{I_k B h_k}{S} + P \frac{dF}{dx} \quad (8)$$

The set of equations (1) to (10) including the equations for mass flow

$$\frac{d}{dx} (\rho u F) = 0; \quad (9)$$

and for state

$$\rho = \sum_i \frac{R}{m_i} \rho_i T \quad (10)$$

and experimental values of  $V_k(x)$ ,  $I_k(x)$  make it possible to calculate gas parameters in the channel.

The calculation of the parameter  $\beta_1$  being dependent of electric field strength is impeded by the field nonuniformity across the channel. This parameter is varied, herefore, in the range of  $0 < \beta_1 < 1$ . But its influence proves to be insignificant because intensive deactivation of  $N_2$  vibrations during V-T relaxation [40 to 43] in the case of collisions with N, O and Na atoms results in equilibrium vibrational and translational degrees of freedom of  $N_2$  molecules. The final calculated data are given at  $\beta_1 \approx 0.5$ .

The parameters  $\beta_1 \approx 0.8$  and  $C_F \approx 5 \cdot 10^{-3}$  were chosen from the conditions of best agreement of calculated pressures  $P_k(x)$  and pressures measured along the electrode wall, and from the correspondence of the value of  $u \times B \times h_k$  to the electromotive force measured on a single remote electrode pair at the channel end.

The set of equations is solved by applying the program for strict differential equations similar to that described in [44]. The program is compiled so that a comprehensive calculation could be performed beginning with the primary nozzle throat and ending with the secondary nozzle exit. In the regions beyond the MHD-channel the equation

$$\frac{d}{dx} \left[ (P + \rho u^2) F \right] = P \frac{dF}{dx} \quad (8')$$

is used instead of (8).

The calculations are conducted until the calculated value of  $P'_0$  coincides with the measured one assuming that the chemical processes are frozen except for vibrational relaxation. Figs. 10, 12, 13 show typical calculated gas parameter distributions along the gas dynamic circuit. The vibrational temperatures in the MHD-channel proved to be close to the translational ones due to an increased rate of vibration deactivation in the presence of O and N atoms. The role of alkali atoms in this process under the conditions in the channel is insignificant. Meanwhile, the chemical gas composition differs slightly from that in equilibrium along almost the whole channel length (Fig. 12).

The high temperature and increased pressure at the channel inlet are caused by shunting the Hall currents which is modelled in the program as energy supply to a gas without its acceleration.

The alkali atoms in the secondary nozzle increase somewhat the gas temperature at the expense of reduction in  $T_{v1}$  (Fig. 13) which causes some variations in the flow Mach number as well.

The extent of correlation of the solutions of one-dimensional equations to real flow parameters depends on the level of energy supply uniformity across the channel, on turbulent mixing processes in the channel etc. These aspects have not been adequately studied at present, although measured pressures  $P'_0$  in the test section indicate the presence of a uniform flow core.

The comparison of flow velocities and the chemical gas composition at the MHD-channel exit calculated by a standard technique and taking into account possible nonequilibrium in the channel, shows that their difference is small. For example, the flow velocity for an equilibrium flow in the MHD-channel is 5100 m/s and that for a nonequilibrium is 4895 m/s. The temperatures are 5700 K and 5720 K, the densities  $1.11 \cdot 10^{-2}$  kg/m<sup>3</sup> and  $1.14 \cdot 10^{-2}$  kg/m<sup>3</sup>, respectively.

The degree of thermochemical process nonequilibrium for flows over models in different wind tunnels was evaluated by using the analog of the Damkohler number [15] in the form:

$$\Psi_i = \frac{L\omega_i}{\rho_\infty u_\infty}; \quad \omega_i = \text{div}(\rho_i U)$$

If  $\Psi < 1$ , the flow is frozen. The case of  $\Psi > 1$  corresponds to an equilibrium flow. At  $\Psi \sim 1$  it is necessary to account for kinetics processes. In the present study, the estimations are performed for nitrogen since it is the main test gas component. For  $\Psi$ , we use the expression from [15] in the form:

$$\Psi_{N_2} = K_{N_2} T^{-1.6} \left[ \exp\left(-\frac{113200}{T_{sh}}\right) \right] \frac{\rho_\infty L}{u_\infty};$$

$$T_{sh} = \frac{2\gamma(\gamma-1)}{(\gamma+1)^2} M^2 T;$$

$$K_{N_2} = 4.8 \cdot 10^{18} C_{N_2} \left( \frac{m^3 K^{1.6}}{kg \cdot s} \right)$$

Models. For tests in all three wind tunnels the following simple configurations were used: a hemisphere plus a cylinder of  $d=40$  mm; a sharp cone with half-angle of  $45^\circ$  plus a cylinder of  $d=40$  mm; a sharp wedge with half-angle of  $30^\circ$  and with a base in the form of a  $30 \times 50 \times 20$  mm<sup>3</sup> parallelepiped. The test models were made of copper to maintain constant model surface temperature and, accordingly, temperature factor. One group of models was covered with 5- $\mu$ m-thick nickel layer by applying non-conductive nickel plating to exclude or, at least, to minimize variations in catalytic model surface activity. Nickel is considered to be a weakly catalytic material but at the same time it is very resistant to exposure of high-temperature chemically-active flow. Catalytic properties of copper surfaces vary considerably when oxide film forms.

The models were tapped to measure pressures. The model design, their dimensions and tapping arrangement are shown in Fig.14. The manufacturing error for linear dimensions is  $\pm 0.05$  mm and that for angular dimensions  $\pm 15''$ . Photos of models are given in Figs.15,16.

In the wind tunnel VAT-102, model pressure distributions were measured by magneto-inductance transducers having flexible diaphragms, the measurement error not exceeding 3%. Visual monitoring was provided in this wind tunnel. In the arc-heating wind tunnel and in the MHD-acceleration wind tunnel, pressure distributions were measured by magneto-inductance transducers and recorded on a computer. For these measurements, error was not also in excess of 3%.

In all three wind tunnels, flow patterns obtained were photographed and filmed. In arc-heating and MHD-acceleration facilities, filming was performed simultaneously via neutral light filters of different intensities and an interference light filter for the wavelength of  $\lambda=4015\text{\AA}$  and transmission band of  $\pm 15\text{\AA}$ . It was established previously that in flow conditions similar to those used in the present study, the effects of advanced and delayed radiation could take place. It was assumed that the radiation with the wavelength of  $\lambda \sim 4000\text{\AA}$  was most likely to correspond to the shock wave front position.

The data obtained by filming were then processed on a computer, the line of maximum radiation gradient being taken as a shock wave boundary.

In single tests carried out in arc-heating and MHD-acceleration facilities the shadow technique was applied to obtain model flow patterns. To do this, a special device was designed and manufactured since it was impossible to use a standard

shadow device because of a low gas density and a high flow glow. This device is based on the effect of abnormal dispersion of resonance radiation with the wavelength of  $\lambda \sim 5890\text{\AA}$  when passing through Na vapor present in the flow.

The device is shown schematically in Fig.17.

The wavelength range for the laser was 4350 to 7300 $\text{\AA}$ , the emission line width required was 0.1 to 0.15 cm, and the beam diameter  $\sim 3$  mm. Maximum impulse frequency ( $\sim 25$  pulse/s) with duration of  $\sim 10^{-8}$  s was used, radiation stability was

approximately  $\sim \pm 10\%$ . The radiation wavelength was checked during tests. Calibration was conducted using a standard lamp CH-8-200 with an interference light filter FWHM of  $\lambda = 0.646 \mu$  and full half-height width of 0.012.

To avoid the influence of possible vibrations occurring during the wind tunnel operation, the optical devices were placed on vibroisolating platforms.

### NUMERICAL TECHNIQUES USED IN THE PRESENT STUDY

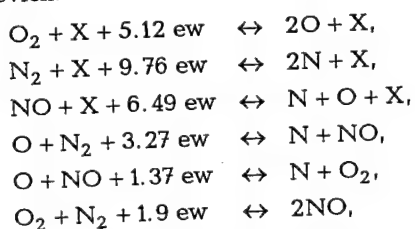
Qualitative characterizations of physical and chemical processes occurring in a shock layer first require numerical calculations. In order to obtain meaningful information, two mathematical models were considered: the theory of a thin viscous shock layer VSL and the method for numerical solution of the full Navier-Stokes equations. Reference free-stream flow parameters contained in the description of test facilities were applied as initial free-stream flow parameters for all three facilities and all test models in the numerical analysis.

#### Numerical simulation of chemically-nonequilibrium hypersonic gas flows by using the equations for a thin viscous shock layer

The set of governing VSL equations [35] includes the equations of continuity, momentum projected onto coordinate axes, energy, conservation for the  $i$ -th component, and the  $j$ -th gas mixture element, the expression for a full heat flux, the equation to calculate diffusive flows including barodiffusion (Stephan-Maxwell relation), the equation of gas mixture state, and the relation expressing the Dalton law. Generalized Rankine-Hugoniot conditions are posed on the external shock wave boundary for the VSL equations. The nonslip and impermeability conditions, the condition of initial heat balance and the catalycity condition are used on the body surface ( $\eta = 0$ ).

The flow profiles in the vicinity of a critical point which result from the solution of self-similar equations on the stagnation line are applied as initial conditions for parabolic equations.

A chemically-nonequilibrium gas model was used in the present investigation to solve the VSL equations. In mathematical modelling of thermochemical reactions, air was considered to be a five-component gas mixture ( $O$ ,  $N$ ,  $NO$ ,  $O_2$ ,  $N_2$ ) and the following six reactions were included according to complex methods developed by Y.B. Zeldovich:



where  $X$  is a catalytic particle which can be represented by any gas mixture component. The constants of equilibrium and rates of return reactions are found here by using the relations recommended in [46]. The given thermochemical model suggests that vibrational degrees of freedom transform instantaneously to a thermodynamic equilibrium state with translational degrees of freedom.

It should be noted that the values of the equilibrium constants have been determined rather accurately. At the same time, there was a significant uncertainty in specifying the expressions for the rates of chemical reactions of dissociation and heat transfer. Therefore, possible influence of these constants on flow characteristics was taken into account in the assessment of the results.

A library of universal programs designed to solve parabolic nonlinear differential equations in an undetailed form was used for numerical integration of the VSL equations describing hypersonic chemically nonequilibrium gas flows over blunt bodies [47]. The two-point second-order Keller scheme was applied for the solution of the VSL equations to approximate the derivatives in the direction normal to the body surface [48]. The advantage of this scheme is that the problem of boundary layer approximation can be easily solved irrespective of grid step ratios. The Keller scheme's nonmonotony was overcome by applying an adaptive grid.

An absolutely stable and fully implicit second-order scheme was used to approximate longitudinal derivatives in the VSL equations. This scheme features good dispersion properties and damps short-wave oscillations of grid functions rather effectively.

The general procedure of solving two- and three-dimensional problems consisted of two stages. The first one included the solution of the self-similar VSL equations on the flow stagnation line by using an adaptive grid for the variable  $\eta$ . A nonuniform grid constructed in the solution of the self-similar problem was fixed in most calculations to use it at the second stage for marching solution of parabolic two- and three-dimensional VSL equations.

The Newton-Raphson method [49] was used for numerical solution of nonlinear grid equations. The correction vector for each iteration of this method was identified by solving linearized equations. The vector factoring was applied to solve linear equations when dealing with one-dimensional (stagnation line) and two-dimensional (separation line) VSL equations.

As for the boundary conditions on the body surface, the wall temperature in all cases was assumed to be  $T_w = 300$  K while the wall itself was assumed to be absolutely noncatalytic.

#### Numerical simulation of hypersonic gas flows over blunt bodies using full Navier-Stokes equations and viscous shock layer equations

Perfect supersonic perfect gas flows over a sphere, a cone and a wedge featuring heat-insulated surfaces were calculated by using the shock-capturing method based on full Navier-Stokes equations [50], [51].

The Navier-Stokes equations in a strictly conservative form were integrated numerically over a finite region limited by external boundary, body surface, plane of symmetry, and exit boundary. The impermeability and nonslip conditions, as well as the condition of heat-insulated body surface were posed on the internal boundary. The dependence of the pressure gradient normal to the surface on the second velocity derivative obtained asymptotically from the momentum equation was used as an additional boundary condition on the body surface. This was required to represent the grid equations in full. The conditions of evenness and oddness for sought functions were posed along the line of symmetry. The conditions of undisturbed flows were used on the external boundary and the conditions of extrapolation of dependent variables on the outflow boundary.

The finite-difference scheme for equations written in the form of conservation laws was based on an integro-interpolation method ensuring the fulfillment of the conservation laws (for the Euler equations even in the presence of discontinuous solutions). The convective flow vector component at half-integer nodes was approximated by using a monotonic second-order scheme [52], [53]. The Roe method for an approximate solution of the problem of the break-down of arbitrary

discontinuity was used to calculate eigenvalues and eigenvectors in half-integer nodes [54]. The diffusive flow vector component was approximated by a linear symmetric difference scheme of the second order. In general, the calculation molecule of the difference scheme on which to approximate full Navier-Stokes equations (including mixed derivatives) included 13 points.

A modified Newton method was used to solve a nonlinear set of grid equations. The Jacobi matrix was formed in each iteration by applying a procedure of finite increments of residual vector in terms of the vector of sought grid functions.

The linear algebraic equations resulted from each nonlinear iteration were solved by factoring the matrix into two triangular matrices L (lower) and U (upper). A preliminary analysis of the sparse structure of matrices L and U was conducted. In order to reduce the total number of arithmetic operations and computer storage loading, the unknown values were renumbered by using the generalized nested dissection method [55].

The procedure of numerical solution of the Navier-Stokes equations by the shock-capturing method is described in more detail in [50], [51].

The most calculations were performed for a  $81 \times 81$  grid. The level of node clustering in radial and azimuth coordinates was chosen depending on the Reynolds number.



# TEST DATA AND THEIR ANALYSIS

The gasdynamic flow parameters used to investigate model flows are summarized in the following tables:

Table 1

Wind tunnel	Gas	$V$ , m/s	T, K	P, Pa	M	R, mm	$Re_0$	$Re_0/Re$	$\Psi$
VAT-102	Nitrogen	790	27	2.6	7.63	20	240	0.1	0
Arc-heating wind tunnel	Air	2695	268	19	7.97	20	150	0.18	$2 \cdot 10^{-10}$
MHD-acceleration wind tunnel	Air	5950	1240	120	7.23	20	135	0.136	0.57

Table 2

Wind tunnel	Gas composition (mole fractions)					
	$N_2$	$O_2$	NO	N	O	K, Na
VAT-102	1.0	-	-	-	-	-
Arc-heating wind tunnel	$7.45 \cdot 10^{-1}$	$1.66 \cdot 10^{-1}$	$4.2 \cdot 10^{-2}$	$1.6 \cdot 10^{-8}$	$3.7 \cdot 10^{-2}$	$10^{-2}$
						0
MHD-acceleration	$5.88 \cdot 10^{-1}$	$3.09 \cdot 10^{-4}$	$5.04 \cdot 10^{-3}$	$6.9 \cdot 10^{-2}$	$3.29 \cdot 10^{-1}$	$10^{-2}$

The model shapes remained unchanged for all test runs since there was no model melting or ablation. When starting arc-heating and MHD-acceleration facilities, oxide copper films appeared on the model surfaces not covered with nickel. It proved to be impossible to control the formation of these films and, therefore, all the main tests were conducted with nickel-coated models. As a result, their surfaces remained clean throughout the balance of testing.

In tests, model surface pressure distributions were obtained, as well as the information about shock wave shapes and stand-off distances.

Figs. 18 - 20 show surface pressure distributions for a hemisphere, a cone, and a wedge. Pressure values are related to respective dynamic pressures  $pu^2$  for the wind tunnel used. For convenience, the data for the wind tunnel VAT-102 are denoted by 1, for the arc-heating wind tunnel by 2, and for the MHD-acceleration wind tunnel by 3. These figures also present theoretical pressure distributions obtained by using different flow models: the VSL theory for perfect gases and gases with physical and chemical processes; and the pressure distribution corresponding to the solution of the Navier-Stokes equation for a perfect gas.

The flow visualization data are presented on photos and video frames showing natural gas glow near models, on shadow pictures for flow fields, as well as on all these pictures after computer processing.

A photo of gas glow over a model obtained in wind tunnel VAT-102 by using glow discharge and its respective video frame are shown in Fig. 21, and photos and video frames of natural gas glow over models in the hypersonic arc-heating and MHD-acceleration wind tunnels in Figs. 22 to 25.

Fig. 26 displays typical computer-processed video pictures for gas glow over models along nitrogen molecule lines.

For ease of comparison with theoretical results, the visualization data for a hemisphere were reduced to dependences of relative shock wave stand-off distances normal to the model surface on relative distances along its surface from the critical point. Cone and wedge data were reduced to dependences of shock stand-off distances normal to their surfaces on distances along the axis from the model nose. Some examples of this data reduction are given in Figs. 27 to 29. Later on, the data of only those runs were used when the influence of model installation inaccuracy was excluded, i.e., when shock stand-off distances for the upper and the lower surfaces coincided.

Figs. 30 to 33 give the summarized flow visualization data for all models tested and the calculated results obtained using VSL theory and the Navier-Stokes equations based on experimental flow parameters for each particular run.

Comparison of experimental and theoretical pressure distributions over a hemisphere (Fig. 18) shows that both for a perfect gas and for a gas with physical and chemical processes the experimental data are in better agreement with the distribution calculated using the Navier-Stokes equations for a perfect gas than with that obtained by VSL theory. The discrepancy becomes appreciable at considerable distances from the critical point which can be attributed to the fact that the Navier-Stokes equations describe flows over a hemisphere in full. There are no terms in the VSL equations which are responsible for convective transfer and diffusion, and the surface pressure distribution is assumed to be corresponded to a modified Newton distribution. The VSL theory is valid only in the vicinity of the forward critical point. This figure also shows that physico-chemical processes in gas have slight influence on the hemisphere pressure distribution. As for a cone and a wedge, the discrepancy for them is more significant (Figs. 19, 20). For a cone, initial pressure values correspond to theoretical ones for a perfect gas (curve 1). The pressure along the cone generatrix decreases quicker than it follows from the Navier-Stokes equations. Respective pressure distribution calculated by VSL theory lies lower than the experimental data. The discrepancy between the theoretical and experimental data is likely to be caused by the fact that the calculation of flows over a cone and a wedge by using the Navier-Stokes equations is performed assuming infinite extension and without accounting for chemical reactions, and the calculation by applying VSL theory proceeding from the above considerations.

The above stated assumptions should be verified in the future by testing models with great relative generatrix lengths and by comparing the data obtained with the calculations using the Navier-Stokes equations including physical and chemical processes.

The analysis of the data on shock wave shapes and stand-off distances for a hemisphere (Fig. 30) shows that for a perfect gas the experimental points lie strictly on the curve calculated by the Navier-Stokes equations. At the same time, the

shock front positions determined according to gas glow boundaries in flow conditions 2 and 3 differ greatly both from each other and from the theoretical

data. The test points for flow condition 2 are lower than the points calculated by the Navier-Stokes equations and somewhat higher than the points obtained by VSL theory; at great distances from the critical point, they essentially lie on the Navier-Stokes curve. At the same time, the shock wave front determined according to gas glow for flow condition 3 is at a greater distance from the body and corresponds to a spherical surface up to angles of  $\sim 50^\circ$ . After that, the test points also lie on the Navier-Stokes curve.

The shock wave position determined from shadow pictures differs significantly from that obtained according to gas glow. On the critical streamline, the shock stand-off distance somewhat exceeds respective value calculated by the VSL theory (Fig. 31), while at great angles, the test points correspond to the NS curve. It follows from these results that the gas glow front near a hemisphere does not correspond to the shock position and is considerably farther from the body especially for flow condition 3.

Similar results are obtained for a cone and for a wedge, but with a less pronounced effect. In flow condition 1, the shock wave position for a cone determined by glow intensity is in good agreement with that calculated by the Navier-Stokes equations; as for a wedge, there is an appreciable discrepancy of measured and calculated values (Fig. 33) which seems to be caused by the fact that the finite wedge width is not taken into account in the NS calculations. As a result, the gas spreads over the wedge width and, consequently, shock waves approach the body. In flow condition 2, the experimental shock front position for a cone obtained by the natural glow intensity coincides essentially with that calculated by the VSL theory. In flow condition 3, the maximum glow gradient front begins in the region of the shock wave front calculated by VSL theory and then shifts to the region calculated by the Navier-Stokes equations. As for the shock wave front determined from shadow pictures, it is higher than that calculated by the Navier-Stokes equations in the initial region for given test conditions and coincides with it at great distances from the nose.

The above considerations show that the application of natural gas glow in flow conditions 2 and 3 is not justified and other optical methods based on different physical principles should be used for flow visualization, for example, a shadow device based on abnormal dispersion effects, methods of resonance fluorescence and so on.

A number of effects were revealed during investigations under review which cannot be explained within the framework of the analysis of such integral characteristics as pressure distributions, shock wave shape and stand-off distances etc. Among them are, first of all, an increased glow region in the vicinity of the critical point for a hemisphere in flow condition 3, a reduced glow near a cone nose etc. It would be possible to assume their dependence on local flow characteristics. To clear up these effects, the test models were calculated within the framework of the VSL theory, and kinetics of vibrational temperatures behind shock waves was analyzed. The fields of temperatures, densities and particle concentrations in shock layers near models were calculated for three flow conditions. The results of these calculations are given in Figs. 34 to 42.

It is seen that there are drastic temperature and density gradients near the hemisphere surface in flow conditions 2 and 3 at distances up to  $\sim 0.1$  of the total shock wave stand-off distance. According to the calculations, the temperature

factor  $T_w/T_0 \approx 0.03$  has an influence only at a very small distance. Similar effects also take place for a cone and for a wedge.

Figs. 36 to 38 show concentration variations of monatomic and molecular components in a shock layer over a hemisphere at different distances from its surface. It is seen that an additional dissociation of nitrogen and oxygen takes place in a shock layer, while recombination processes begin to take effect only in the close vicinity of a cold wall. Of importance is a drastic variation in NO concentration along streamlines. Similar results are obtained in shock tunnel tests. As stated above, the excitation of electron states of NO molecules causes an intensive ultraviolet glow from this flow region [6].

On the other hand, monatomic components of N and O would result in a certain influence of the catalytic level on shock stand-off distances [16]. In the given investigations, the influence of catalytic level on shock stand-off distances is not considered. Moreover, nickel featuring weak catalytic properties is chosen deliberately for model surfaces.

A possible difference of the glow front position from the shock front may be explained by two mechanisms: by removal of glow from the shock layer region basically in the form of resonance radiation and by emission of high-energy electrons from a high-temperature region immediately adjacent to the shock wave front. These two phenomena can result in an excitation of electron states of impinging molecules and atoms of air and seeds which may be attributed to the presence, in flow condition 3, of a sharp front boundary of the glow region at the critical point of a hemisphere and its spherical character up to angles corresponding to the transition of a subsonic region to a supersonic one. The effects of radiation removal are characteristic of strong shock waves caused, for example, by nuclear explosion [56] or of meteors entering the atmosphere [57].

The situation close to the flow condition considered here is discussed in [58]. Based on numerical solution of the Biberman equations for radiation diffusion in resonance lines it is shown that the effect observed may be explained by radiation transfer in resonance lines Cu and Na with their subsequent reradiation to the region ahead of the shock wave. In flow condition 3, the above effects take place not only for seeds having a small excitation potential but also for nitrogen and oxygen. The analysis of these processes is beyond the scope of this study.

The numerical estimates of characteristic electron free-path lengths as applied to the conditions of emission from a high-temperature gas show that they are of  $\sim 2$  mm, i.e., they are close to experimental glow zone dimensions. It is known, on the other hand, that a body moving with velocities of  $\sim 5-6$  km/s can gain electric charge of a order of several V [59] which also contributes to electron emission.

In conclusion, consider the following point. An obligatory condition of the MHD-acceleration wind tunnel operation is the presence of alkali seeds in the flow. In the given tests, seeds were used in single runs and in the arc-heating wind tunnel. Although their small

fraction ( $\sim 1\%$  of weight) could not, naturally, change thermodynamic gas parameters (pressure, enthalpy, heat conductivity etc.) they could influence rates of relaxation processes. In order to clarify this point, methods of mathematical modelling were applied to investigate translational and vibrational temperature distributions, as well as air component concentrations behind a normal shock wave and shock waves being at angles of  $51^\circ$  and  $38^\circ$  to the flow. The last condition corresponded to test shock wave positions for a cone and for a wedge, respectively.

The calculation was performed for the same free-stream flow parameters without Na and K and with them. The concentration was assumed to be equal to ~1% with respect to gas mass flow rate. The calculated results are given in Figs. 43, 44 .

It is seen that in the case of a normal shock wave, the seeds exert a very small influence on thermodynamic processes. The attainment of thermodynamic equilibrium at given parameters required  $\sim 10^{-4}$  s. The influence of seeds on relaxation of vibrational degrees of freedom is most appreciable behind shock waves near a wedge and a cone. But in this case, their influence on thermodynamic processes (P, T) is insignificant (Fig. 44). Some displacement of the nitrogen vibrational temperature maximum relative to translational one can result in displacement of a radiation front relative to a shock wave since electron temperature is governed here by vibrational temperature. This phenomenon can be a cause of radiation delay in flow condition 3 near a cone nose (Fig. 32) and it is likely to be attributed to the coincidence of the shock wave determined by the shadow technique with that calculated using the Navier-Stokes equations for a perfect gas. Indeed, the shock wave position for a fully frozen gas would correspond to a flow with  $\gamma=1.48$ . Due to relaxation of vibrational degrees of freedom the quantity  $\gamma$  decreases and approaches a value close to 1.40. The fact that the shock wave stand-off distance in the vicinity of cone nose is greater than that followed from the Navier-Stokes equations confirms this phenomenon since in this case the flow in the cone nose vicinity is close to a frozen one.

## CONCLUSION

Flows over simple bodies (a hemisphere, a cone, a wedge) have been investigated in wind tunnels of different types at close similarity parameters for Mach and Reynolds numbers but at essentially different flow velocities. The tests were carried out in the vacuum wind tunnel VAT-102 for the conditions of a perfect gas ( $u = 790$  m/s,  $M = 7.63$ ,  $Re_0 = 240$ ,  $H_0 = 0.32$  MJ/kg), in the arc-heating wind tunnel in a gas flow featuring excited vibrational degrees of freedom and a small dissociation level ( $u = 2700$  m/s,  $M = 7.97$ ,  $Re_0 = 150$ ,  $H_0 = 5.2$  MJ/kg) and in the MHD-air flow acceleration where the influence of physical and chemical processes can be significant ( $u = 5950$  m/s,  $M = 7.23$ ,  $Re_0 = 135$ ,  $H_0 = 29$  MJ/kg).

The matched operation conditions of the facilities used and the means of their checking were optimized during the tests by applying the technique of determining both gasdynamic ( $M$ ,  $Re$ ,  $Re_0$ ,  $T$ ,  $P$ ,  $U$ ,  $H_0$ ,  $H$ ) and physical and chemical ( $\gamma$ ,  $T_0$ ,  $T_{v_1}$ ,  $T_{tr}$ ,  $C_i$ ) free-stream flow parameters. Particular attention was given to the influence of nonequilibrium processes in a gas accelerated in the MHD-channel of the hypervelocity wind tunnel and in the secondary nozzle. It was shown that nonequilibrium effects are insignificant in the MHD-channel. The flow in the secondary nozzle is closer to a frozen one; alkali seeds, being in air flow, approach the thermodynamic gas to an equilibrium state mainly by accelerating deactivation of vibrational degrees of freedom of nitrogen.

Different means of flow visualization are devised and tried. They are based on recording of flow glow near models excited by glow discharge electrons (VAT-102) or natural flow glow (arc-heating and MHD-acceleration wind tunnels). Both neutral and interference light filters were used in the MHD-acceleration wind tunnel. A shadow device has been developed based on the effect of abnormal dispersion of Na atom resonant radiation with the application of an impulse laser of variable radiation frequency as a light source. This made it possible to increase the device sensitivity by a factor of 10 and to exclude distortions due to shock wave front glow.

Pressure distributions over model surfaces were measured in all wind tunnels used and compared with calculations performed for test conditions by applying the VSL theory and the Navier-Stokes equations.

As for a hemisphere, the influence of the flow velocity on the pressure distribution over its surface has not revealed and in all cases it was in good agreement with that calculated using the Navier-Stokes theory by the VSL theory and Navier-Stokes equations.

Thus, a number of new effects have been revealed during the investigations carried out which cannot be explained in the framework of integral characteristics. It seems to be possible that they depend on local shock layer parameters. To verify this suggestion, they were calculated by applying the VSL theory; the influence of alkali seeds on relaxation rate was analyzed. Some fields of gasdynamic parameters ( $P, \gamma, T, U$ ) and chemical air component concentrations ( $O$ ,  $N$ ,  $NO$ ,  $N_2$ ,  $O_2$ ) were obtained. It is shown that  $N_2$  and  $O_2$  dissociate in a considerable region of the shock layer and their recombination occurs only near the cold wall, the influence of temperature factor being small. A sharp peak of  $NO$  concentration is observed which can be a source of an intensive nonequilibrium ultraviolet radiation. In addition, the available high-temperature region is a source of rapid electrons. Both

these factors can cause radiation removal for a distance behind the shock wave front.

It is shown that seeds of ~1% behind a normal shock wave do not influence the chemical reaction rate and vibrational temperature relaxation, and behind an oblique shock wave (cone, wedge) its influence is very weak (~2 to 3%). But behind an oblique shock wave the vibrational temperature maximum is farther away from the shock wave front because of a greater gas velocity which can shift the radiation intensity peak closer to the body surface.

The results obtained also show that it is important to choose a required gasdynamic model. It follows from the comparison of theoretical and experimental data that the flow model based on the Navier-Stokes equations is in better agreement with the test results than that calculated using the VSL theory. Therefore, the multitemperature kinetics of chemical reactions in air should be considered within the framework of the Navier-Stokes equation solution. The reproduction of a stationary flow field over a model and that repeated from run to run allows the statement of a problem concerning the evaluation of a detailed structure of the shock layer, i.e., chemical air component distribution in the layer, both equilibrium and nonequilibrium radiation intensity and spectrum.

It seems to be reasonable to evaluate the influence of the model surface catalycity level on the shock wave stand-off distance and the flow character. The capabilities of available hypervelocity wind tunnels and other hypersonic wind tunnels of TsAGI make it possible to carry on similar experimental investigations of greater models at considerably higher Mach numbers  $M=15$  to  $20$  but at slightly less Reynolds numbers  $Re_s=50$  to  $100$ .

#### ACKNOWLEDGEMENT

The authors are deeply indebted to EUROPEAN OFFICE of AEROSPACE RESEARCH and DEVELOPMENT (EOA RD) for the opportunity granted to conduct these investigations and to the collaborators of WL WRIGHT PATTERSON AFBOH for their attention and support.

# NOMENCLATURE

b	accelerator channel width
B	magnetic field induction
$C_f$	channel drag coefficient
$C_i$	concentration of i-particles (mole fractions)
d	diameter
D	hydraulic diameter
E	energy
$E_v$	vibrational energy
$E_{vi}$	vibrational energy per i-particle
E	electric field strength
$\mathcal{E}_i$	energy required to generate i-component
F	channel cross-section area
j	current density
h	channel height
H	enthalpy
I	current
$\mathcal{I}_i$	function of generation of i-particles
L	characteristic size, channel length
m	molecular weight
$\dot{m}$	gas mass flow rate
M	Mach number
P	pressure
Q	heat flux related to unit volume
r	coefficient responsible for electrode current nonuniformity [30]
R	radius
R	universal gas constant
$Re = \frac{\rho_\infty u_\infty L}{\mu_\infty}$	Reynolds number
$Re_0 = \frac{\rho_\infty u_\infty L}{\mu_0}$	Reynolds number based on stagnation parameters
S	channel (electrode) sectioning step
T	temperature
u	velocity
V	measured electrode-to-electrode voltage



$\Delta V_{\text{near}}$	near-electrode voltage drop
X	coordinate along flow
Y	coordinate across flow normally to applied magnetic field B
$Z_i$	energy transfer rate to vibrations of i-particles
$\beta$	total energy fraction supplied to gas
$\beta_1$	total energy fraction transferred to $N_2$ molecules
$\beta_H = \omega\tau$	Hall parameter
$\gamma$	specific heat ratio
$\delta$	shock wave stand-off distance
$\mu$	viscosity
$\rho$	density
$\sigma$	electric conductivity
$\tau$	characteristic time
$\Psi = \frac{\omega_i L}{\rho_\infty u_\infty}$	Damkeller number
$\omega$	circular frequency
$\omega_i$	source term in chemical reaction for i-particles

#### Subscripts

aerod	aerodynamic
chem	chemical
c	core
diss	dissociation
d	drop
e	electrode
eq	equilibrium
fr	frozen
g	gas
H	Hall
$i = 1, 2, 3, 4, 5, 6$ refer to $N_2, O_2, NO, O, N, Na$ , respectively	
k	electrode number
m	model
n	full-scale
o	total (stagnation)
Tr	translational
V	vibrational
vtr	vibrational-translational
VV'	vibrational-vibrational
x	streamwise
y	across flow
w	wall

## REFERENCES

1. Rakich J.V., Baiby H.E. and Park G., Computation of Nonequilibrium Supersonic Three-Dimensional Inviscid Flow over Blunt Nosed Bodies, AIAA Journal, vol.21, N6, 1983
2. Candler G. and MacCormac, The Computation of Hypersonic Inviscid Flows in Chemical and Thermal Nonequilibrium, AIAA Paper, N88-0511, 1988
3. Afonina N.E., Gromov V.G., Some Results of Numerical Investigations of Gasdynamics and Heat Transfer for Bodies of Complicated Shapes in a Supersonic Air Flow, Gagarin Readings on Aeronautics and Aviation, 1989, Nauka, Moscow (in Russian)
4. Park C. Assessment of Two Temperature Kinetic Models for Ionizing Air, AIAA Paper, N87-1574, 1987
5. Jaffe R.L. Rate Constants for Chemical Reactions in High-Temperature Nonequilibrium Air. Progress in Astronautics and Aeronautics: Thermophysical Aspects of Reentry Flows, vol.103 edited by J.N. Mess and C.D. Scott, American Institute of Aeronautics and Astronautics, New York, 1985
6. Wurter W.H., Trenor C.E. and Williams M.J., Kinetics of UV Production behind Shock Wakes in Air, AIAA Paper, N90-1666, 1990
7. Camm J.C., Kivel R.L., Taylor R.L. and Tear J.D., Absolute Intensity of Nonequilibrium Radiation in Air and Stagnation Heating of High Altitudes, AVCO Everett Research Laboratory, Everett M.A. Research Report N93, 1959
8. Davies C.B. and Park G., Aerodynamic and Thermal Characteristics of a Modified Blunted Cone, AIAA N86-1309, 1986
9. Hunt J.L. Measured Pressure Distribution on Large-Angle Cones in Hypersonic Flows of Tetrafluoromethan, Air and Helium, NASA TN D-7429, 1973
10. Hunt J.L. et al, Investigation of Real Gas and Viscous Effect on the Aerodynamic Characteristics of 40 Half Cone with Suggested Correlations for the Shuttle Orbites, NASA TN D-8418, 1977.
11. Sharma S.R. and Park G., A Survey of Simulation and Diagnostic Techniques for Hypersonic Nonequilibrium Flows, AIAA Paper N87-0406, 1987
12. Compton H.R., Saffion W.J., Suit W.T., Schiess J.R., Shuttle Entry Performance and Stability and Control Derivatives Extracted from Flight Measurement Data, AIAA Paper N82-1317, 1982
13. Lobb R.K., Experimental Measurement of Shock Detachment Distance on Spheres Fired in Air at Hypervelocities in "The High Temperature Aspects of Hypersonic Flow", ed. W.C. Nelson Pergamon Press MacMillan Co, New York 1964
14. Stuckert G.K. and Reed H.L. Stability of Hypersonic, Chemically Reacting Viscous Flows, AIAA Paper N90-1529, 1990
15. Candler G., On the Computation of Shock Shapes in Nonequilibrium Hypersonic Flows, AIAA Paper N89-0312, 1989
16. Alforyov V.I., Rudakova A.P., Shakhmatov V.A., Shchelin V.S., mathematical Simulation of a Shock Layer Structure Near a Model in Wind Tunnels, Matematicheskoye Modelirovanie, vol. 1, N9, 1989 (in Russian)
17. Alforyov V.I., Vitkovskaya O.N., On Simulation of Hypervelocity Flows over Bodies in Wind Tunnels, Izv. AN SSSR, Mekhanika Zhidkosti i Gaza, N1, 1983, (in Russian)
18. Alforyov V.I., Vitkovskaya O.N., Rudakova A.P., Rukavets V.P., Shcherbakov G.I., Gasdynamic Wind Tunnel with MHD-Gas Acceleration, X International

- Conference on Magnetohydrodynamic Electric Power Generation, India, vol.1, VII, 1989
19. Alforyov V.I. A Report on Status of MHD Hypersonic Ground Test Technology in Russia, AIAA Paper N93-3193, 1993
  20. Alforyov V. On the Problem of Creating the Flow Conditions in Scramjet Combustion Chamber in Wind Tunnels, AIAA Paper N93-1943, 1993
  21. Illarionova L.G., Lipin A.V., Low-Temperature Vacuum Wind Tunnel, Collection of VINI MPS TTE, Series "A", issue N10, 1984 (in Russian)
  22. Lederer M., Janta W. and Ragsdale W., Condensation in Hypersonic Nitrogen Wind Tunnels, AIAA Paper N90-1392, 1990
  23. Alforyov V.I., Vitkovskaya O.N., Ustinov Yu.S. Shcherbakov G.I., Arc-Heater with an Arc Rotated by Magnetic Field, TVT, vol.9, N2, 1971 (in Russian)
  24. Shcherbakov G.I., Electric Discharge Between Coaxial Electrodes in Transverse Magnetic Field, Trudy TsAGI, issue 1949, 1979 (in Russian)
  25. Alforyov V.I., Vitkovskaya O.N., Rykavets B.P., Shcherbakov G.I., MHD-Gas Flow Acceleration Wind Tunnel, TVT, Vol.1, N1, 1979 (in Russian)
  26. Stolyarov Yu.V., Shcherbakov G.I., A Device for Supplying Liquid Alkali Metals to an Aggressive Gas Flow, Invention Certificate N953896, 1982 (in Russian) 1982
  27. Stolyarov Yu.V. Shcherbakov G.I., A Source of Conducting Gas for a Hypersonic Wind Tunnel, Invention Certificate, N1602377, 1989 (in Russian)
  28. Labazkin A.P. Turchannikova L.S., Shvetsov B.A., Shcherbakov G.I., The MHD-channel, Invention Certificate N1741589, 1991 (in Russian)
  29. Vitkovskaya O.N. Rudakova A.P., Calculation of the MHD-accelerator Air Flow with Taking Account of the Channel Drag and Heat Transfer in the Wall, Uchenye Zapiski TsAGI, vol.5, N4, 1974 (in Russian)
  30. Selinsky , Fisher , The Influence of Electrode Sizes on Parameters of MHD-Generators with Sectionized Electrodes, PTK, N3, 1966 (in Russian)
  31. Zdunkevich, M.D., Sevastyanov R.M., A Standard program for Calculations of Thermophysical Air Properties, Trudy TsAGI, issue 1009, 1966 (in Russian)
  32. Zdunkevich M.D., Sevastyanov R.M., Chernavskaya R.A., Electric Conductivity of Nitrogen with Seeds of Readily-Ionized Metal Vapors in a Magnetic Field, Trudy TsAGI, issue 1010, 1966 (in Russian)
  33. Alforyov V.I., Vitkovskaya O.N., Rudakova A.P., Shcherbakov G.I., The Investigation of Electrodynamical characteristics of MHD-Accelerator, TVT, vol.17, N2, 1979 (in Russian)
  34. Labazkin A.P., The Experimental Investigation of the Temperature Fields and Heat Fluxes over the Electrode Walls of the High-Enthalpy MHD-Channel.- X International Conference on Magnetohydrodynamic Electric Power Generation. Tirchi, India, vol.1, 1989
  35. Krivonosova O.E., Losev S.A., Nalivayko B.P., Mukoseyev Yu.K., Shatalov O.P., The Recommended Data on Rate Constants of Chemical Reactions between Molecules Consisting of N and O Atoms, Khimiya Plasmy, Energoatomizdat, Moscow, issue 14, 1987 (in Russian)
  36. Banech D.L., Drysdale D.D., Horne D.C. Evaluated Kinetic Data for High Temperature Reactions, vol.2. Homogeneous Gas Phase Reactions of the H<sub>2</sub>-N<sub>2</sub>-O<sub>2</sub> System. London: Butterworths, 1973
  37. Camac M., Feinberg R.M. - 11-th Combustion Symp. 1967
  38. Park C. Review of Chemical-Kinetic Problems of Future NASA Missions, In: Earth Entries - J. of Thermophysics and Heat Transfer, vol.7, N3, 1993
  39. Biryukov A.S., Kinetics of Physical Processes in Gasdynamic Lasers, Trudy FIAN, vol.83, 1975, (in Russian)

40. Fisher E.R., Smith G.K. Alkali Quenching in High Temperature Environment, Chem. Phys. Lett., vol.13, N5, 1972
41. Andreev E.A. - Chem. Phys. Lett., vol.23, 1973
42. Eremin A.V., Kulikovskii A.A., Naboko I.M. - Chem. Phys. Lett., vol.45, N2, 1977
43. Breyev V.V., Gubarev A.V., Panchenko V.P., Supersonic MHD-Generators, Ed. Gubarev A.V., Energoatomizdat, Moscow, 1988 (in Russian)
44. Gear C.W. Numerical Initial Value Problems in Ordinary Differential Equations. - New York, 1971
45. Cheng H.K. Hypersonic Shock-Layer Theory of the Stagnation Region at Low Reynolds Number. - Proc.1961, Heat Transfer and Fluid Mech. 1961
46. Kang S.W., Dunn M.C. Theoretical and Measured Electron-Density Distribution for the RAM Vehicle at High Altitudes. - AIAA Paper N72-689, 1972
47. Babikov P.E., Yegorov I.V. On One Version of the Adaptive Grid Generation to Solve Evolution Problems, Proc. Soviet Union-Japan SCFD, vol.2, 1988
48. Keller H.B., Cebest T. Accurate Numerical Method for Boundary-Layer Flow. II. Two-dimensional Turbulent Flows, AIAA Journal, vol.10, 1972
49. Pletcher R.H., Daney C.L. A Direct Method of Calculating through Separated Regions in Boundary Layer Flow, Journal Fluids Engin., vol.98, 1976
50. Yegorov I.V., Zaitsev O.L., On One Approach to a Numerical Solution of Two-Dimensional Navier-Stokes Equations by Using Shock-capturing Method, Zh. Vychisl. Matem. i Matem. Fiz., vol.31, N2, 1991 (in Russian)
51. Yegorov I.V. and Zaitsev O.L. Development of Efficient Algorithms for Computational Fluid Dynamics Problems. Proc. of the 5th International Symposium on Computational Fluid Dynamics, Sendai, Japan, vol.3, 1993
52. Kolgan V.P. The Application of the Principle of Minimum Derivative Values to the Construction of Finite-Difference Schemes to Calculate Discontinuous Solutions of Gas Dynamics, Uchenye Zapiski TsAGI, vol.3, N6, 1972 (in Russian)
53. Harten A. High-Resolution Schemes for Hyperbolic Conservation Laws, J. of Computational Physics, vol.49, 1983
54. Roe P.L. Approximate Riemann Solvers, Parameter Vectors, and Difference Scheme, J. Comput. Phys., vol.43, 1981
55. Lipton R.J., Rose D.J., Tarjan R.E. Generalized Nested Dissection, SIAM J. Numer. Anal., vol.16, N2, 1979
56. Zeldovich Ya. B. Raizer Yu.P., Physics of Shock Waves and High-Temperature Phenomena, Nauka, Moscow, 1967 (in Russian)
57. Bronshtein V.A., Physics of Meteor Phenomena, Nauka, Moscow, 1981 (in Russian)
58. Alfeyorov V.I., Sklyarov, K.Yu., Shinelev A.A., Mathematical Simulation of Radiation Removal from the Region of a Strong Shock Wave, Matematicheskoye Modelirovaniye, vol.3, N9, 1991 (in Russian)
59. Piljugin N.M., Measurement of Electric Discharges Near Bodies in Hypersonic Motion, TVT, vol.32, N1, 1991 (in Russian)

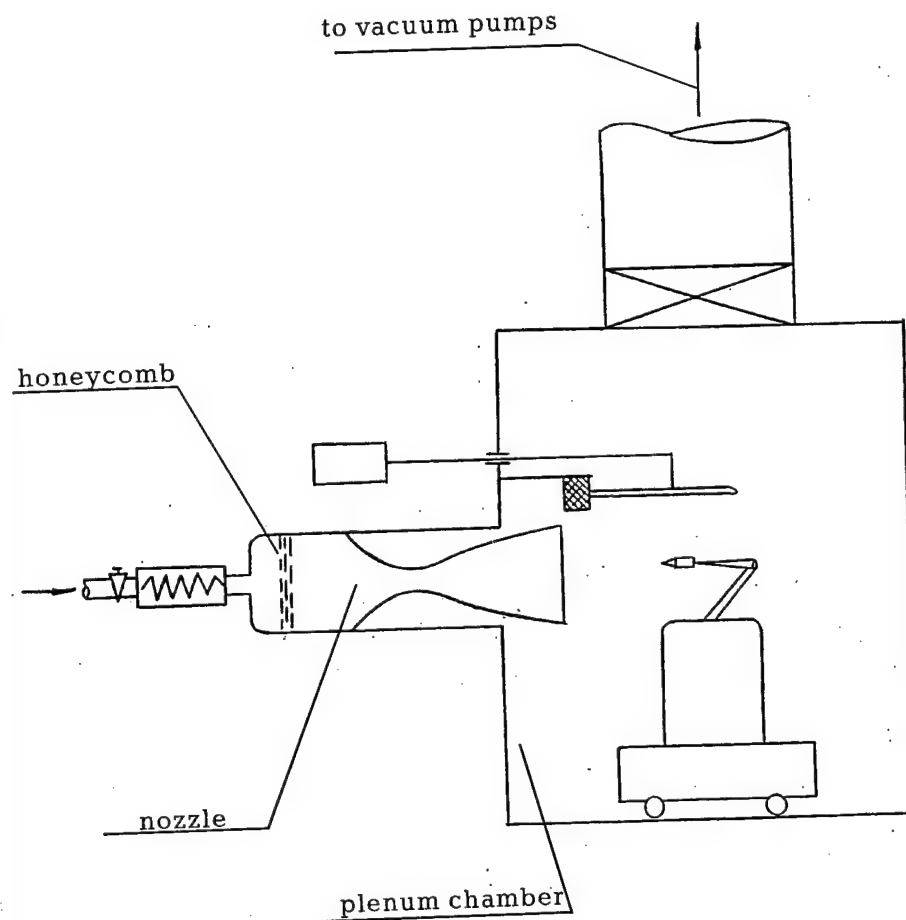


Fig.1. Hypersonic low-density vacuum wind tunnel VAT - 102.

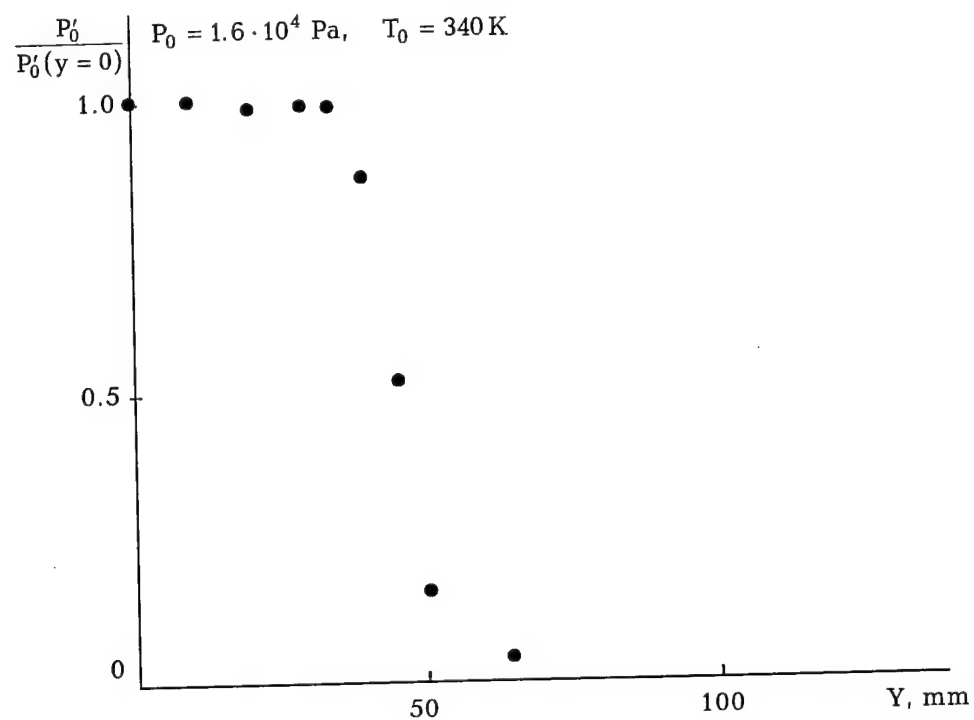


Fig.2. Pressure field  $P'_0$  VAT - 102.

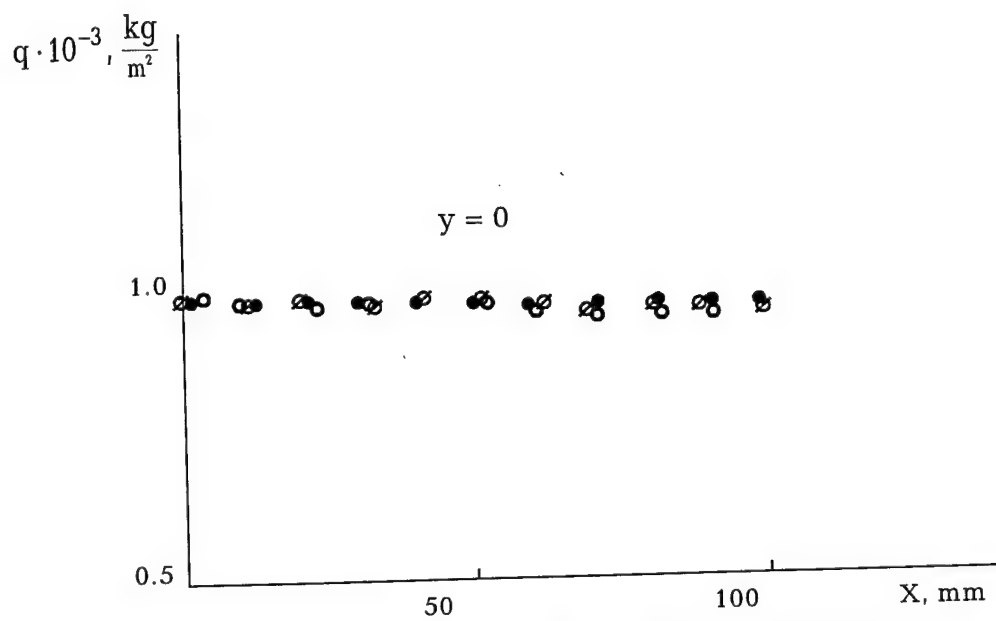


Fig.3. Dynamic pressure distributions along the nozzle axis.

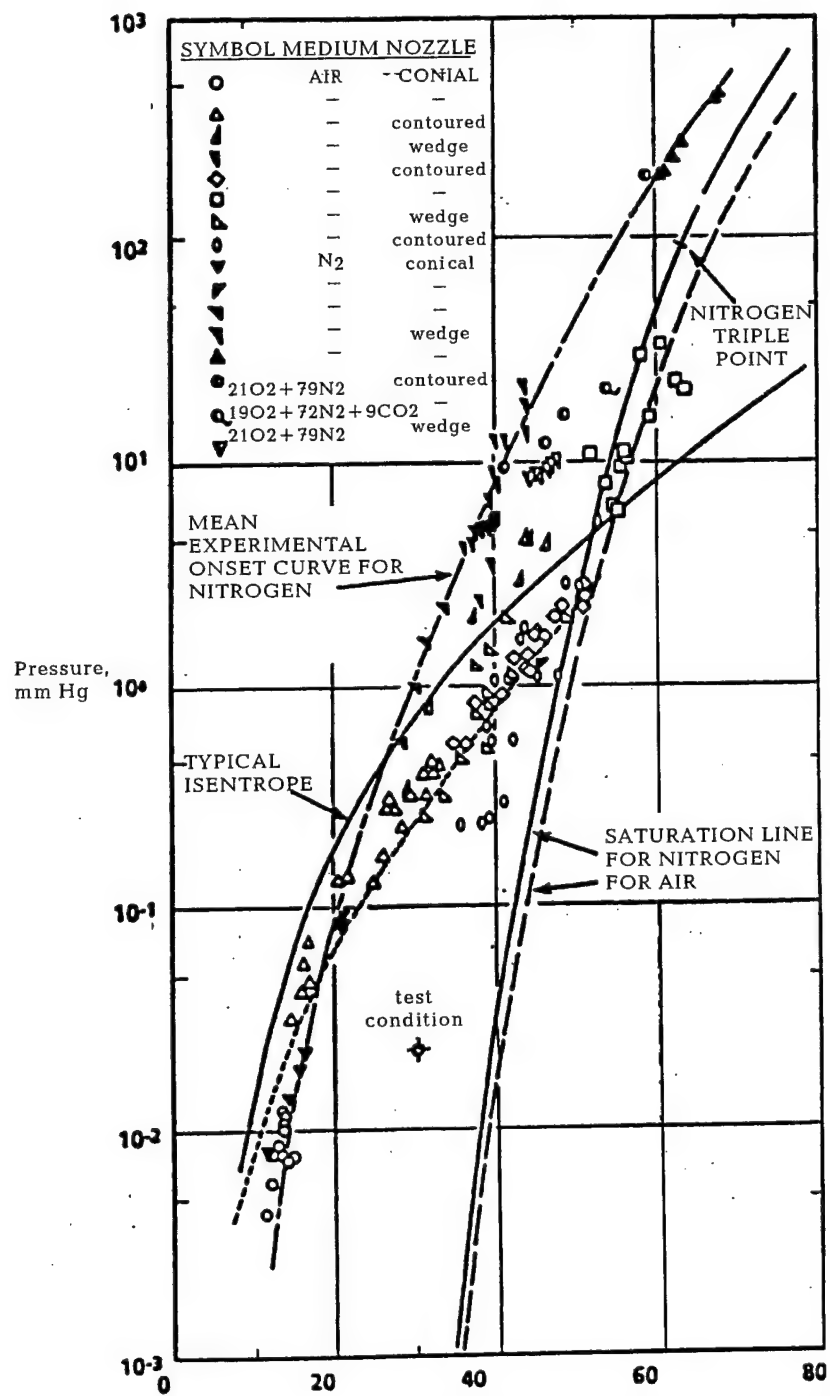


Fig.4. Comparison of air and nitrogen condensation.

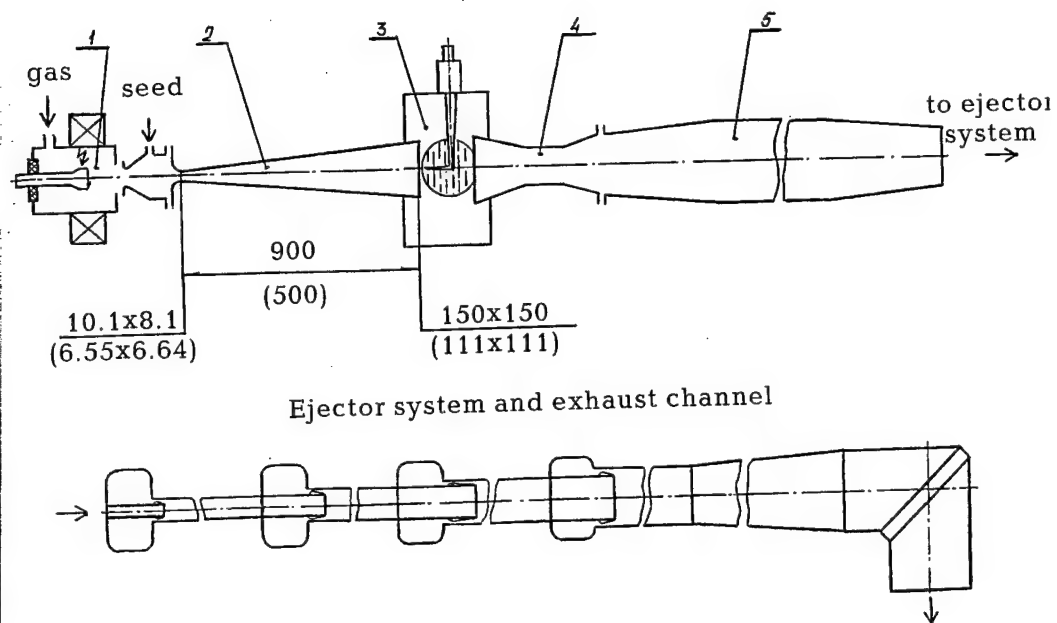


Fig.5. Hypersonic arc - heating wind tunnel

- 1 - arc - heater;
- 2 - nozzle;
- 3 - test section;
- 4 - supersonic and subsonic diffusers;
- 5 - cooler



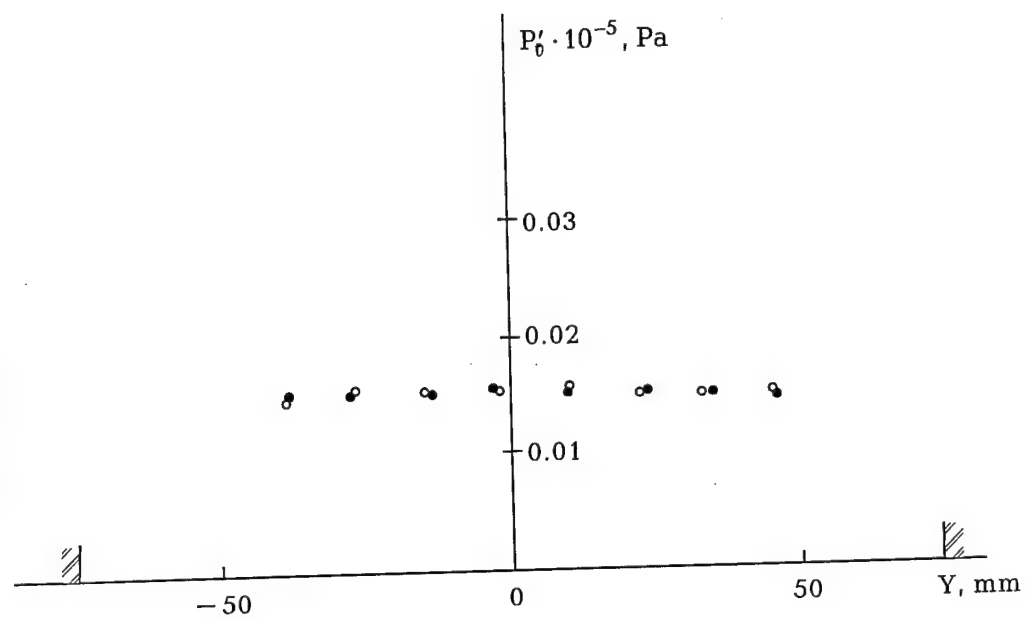


Fig.6. Pressure field  $P'_0$ . Hypersonic arc - heating wind tunnel.

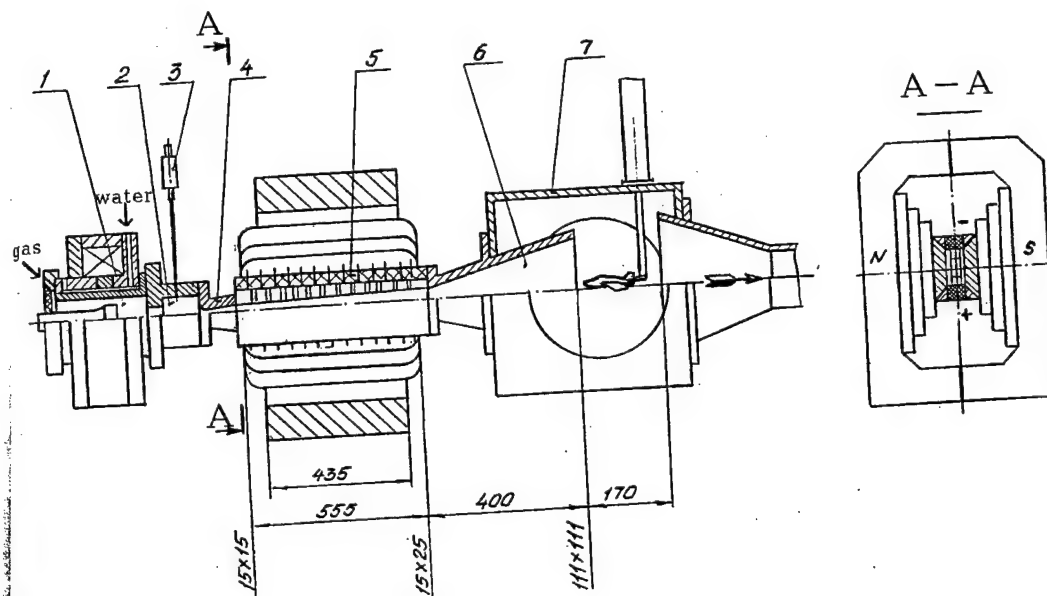


Fig. 7. Schematic of hypervelocity MHD - gas acceleration wind tunnel

- 1 - arc - heater;
- 2 - mixing chamber;
- 3 - metering device;
- 4 - primary supersonic nozzle;
- 5 - MHD - accelerator;
- 6 - secondary nozzle;
- 7 - test section

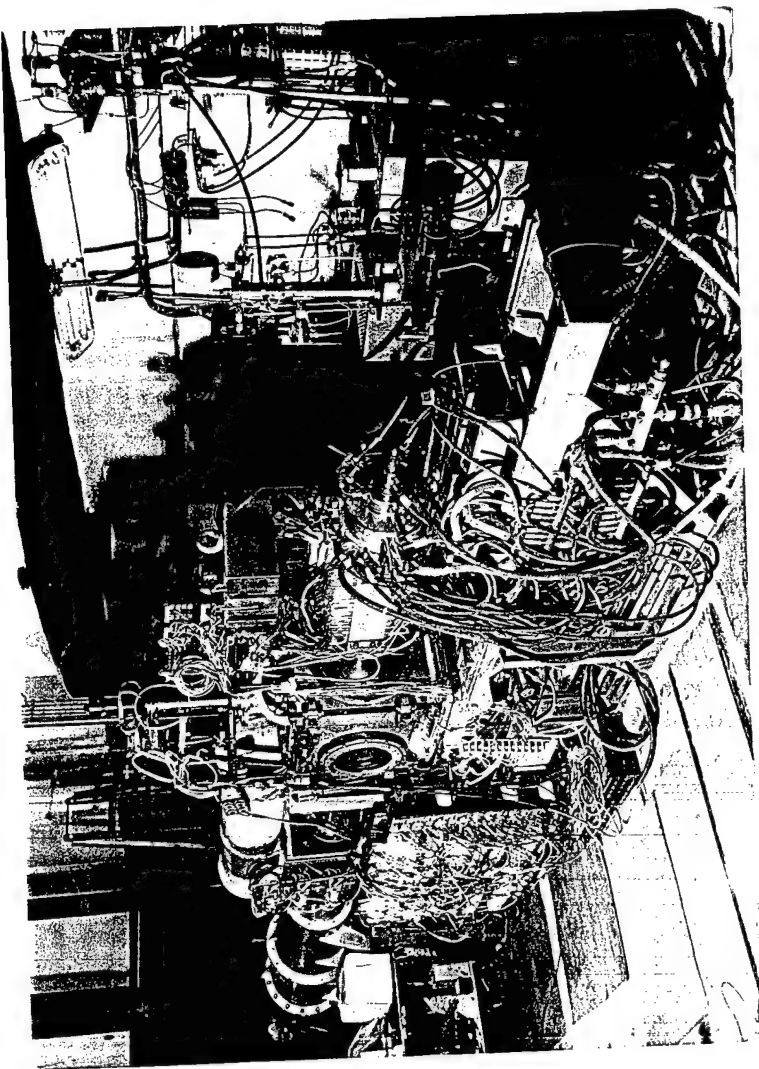


Fig.8. Hypervelocity MHD - gas acceleration wind tunnel. General view.

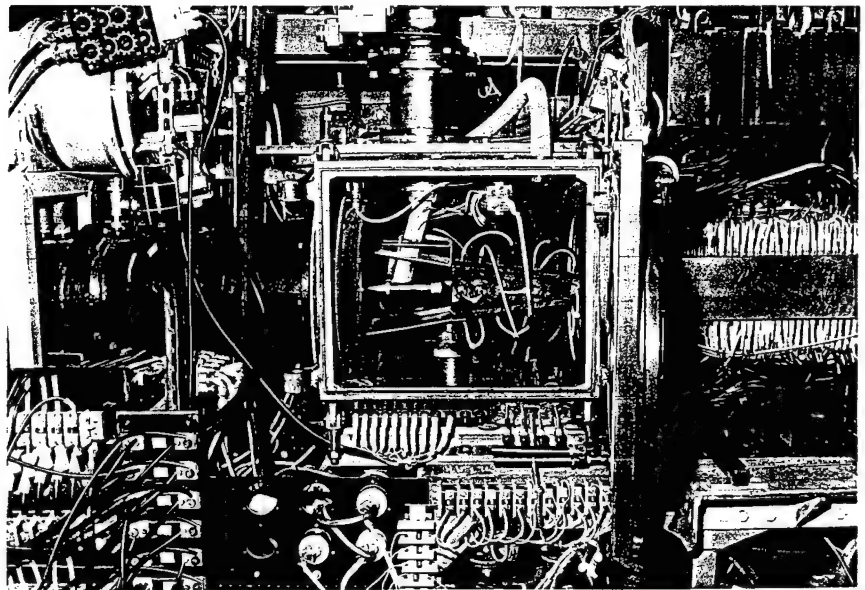
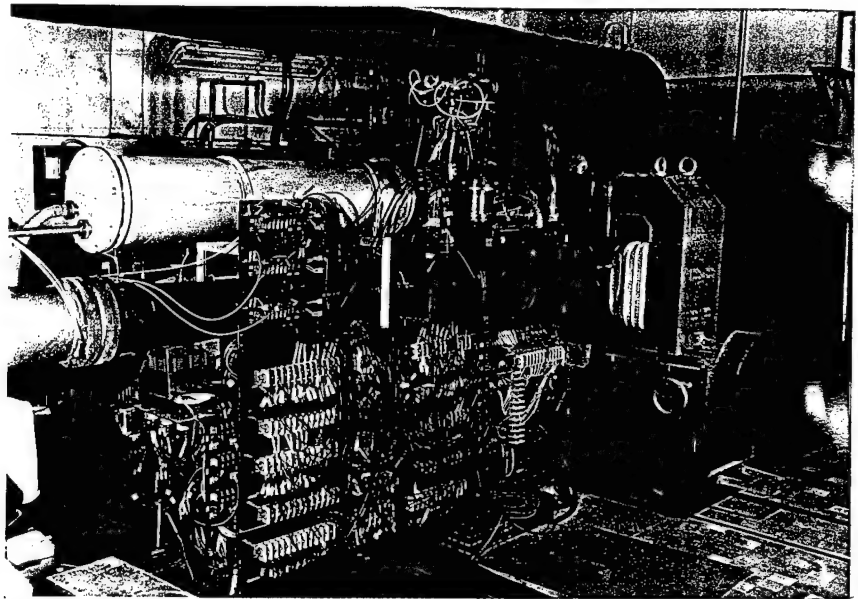


Fig. 9. Hypervelocity MHD—gas acceleration wind tunnel. General view.

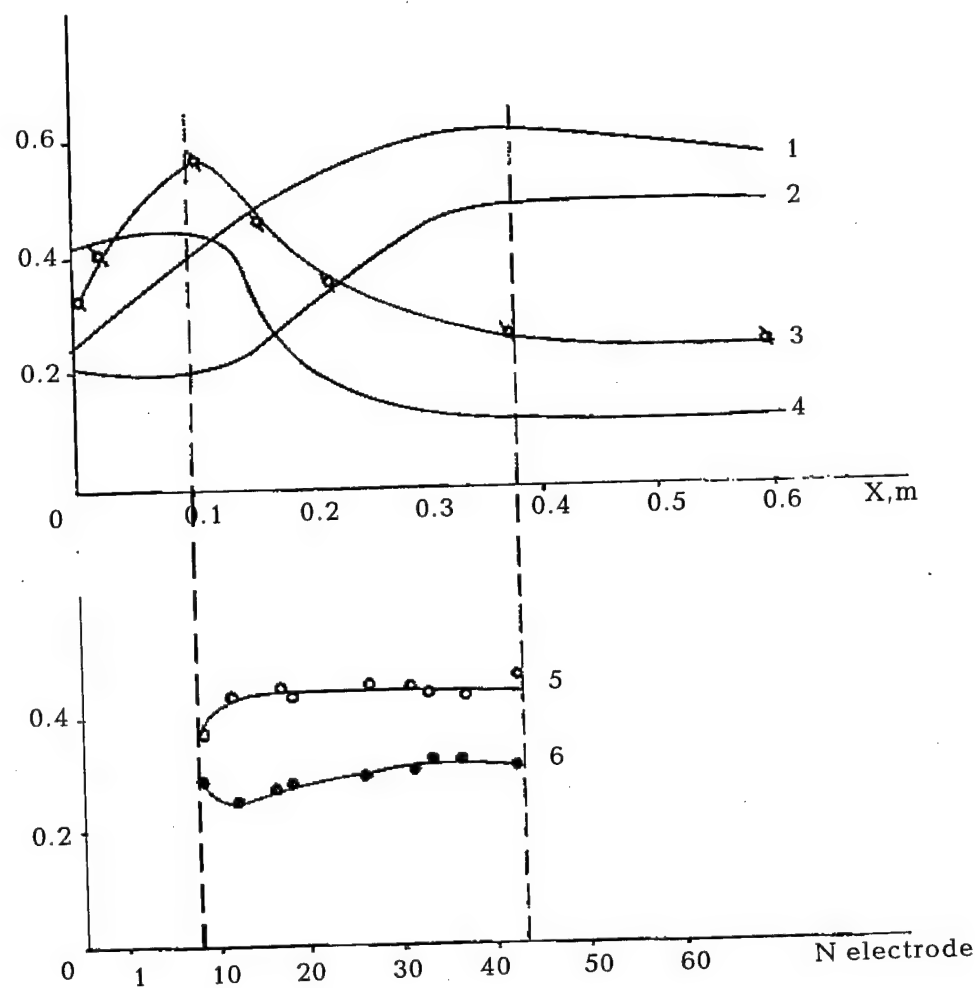


Fig.10. Electric and gasdynamic parameter distributions along the accelerator channel

- 1 - temperature;  $T \cdot 10^{-4}, K$
- 2 - velocity;  $u \cdot 10^{-4}, m/s$
- 3 - static pressure;  $P \cdot 10^{-5}, Pa$
- 4 - density;  $\rho \cdot 10^1, kg/m^3$
- 5 - electrode current;  $I \cdot 10^{-2}, A$
- 6 - electrode voltage;  $V \cdot 10^{-3}, m/s$

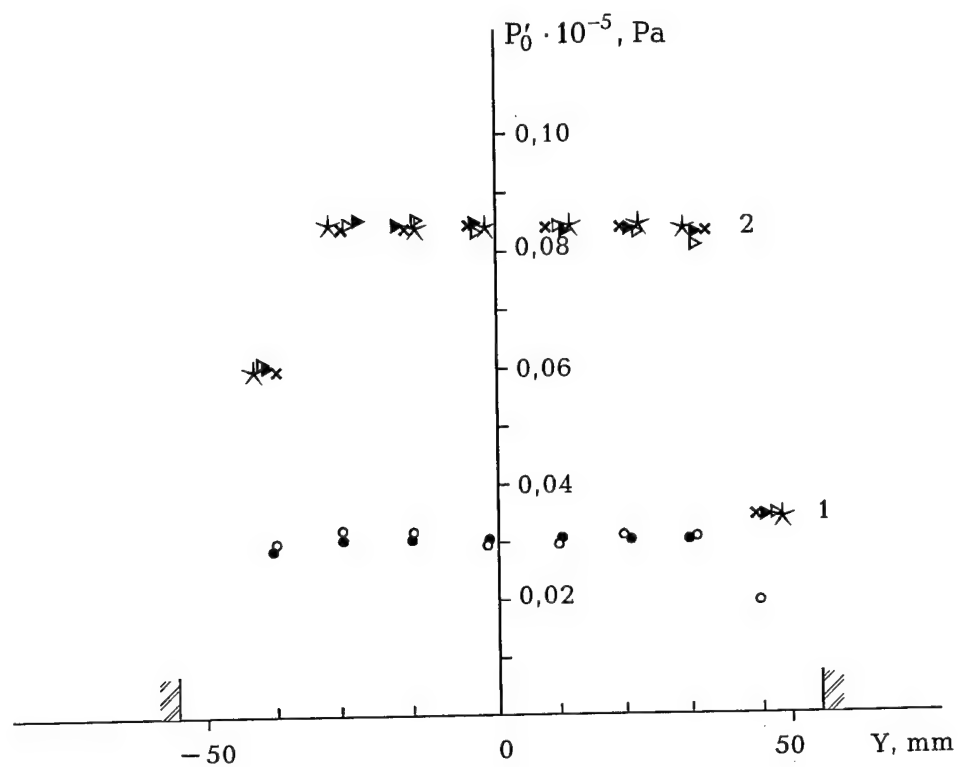


Fig.11. Pressure field  $P'_0$

1 — without MHD — acceleration; 2 — with MHD — acceleration

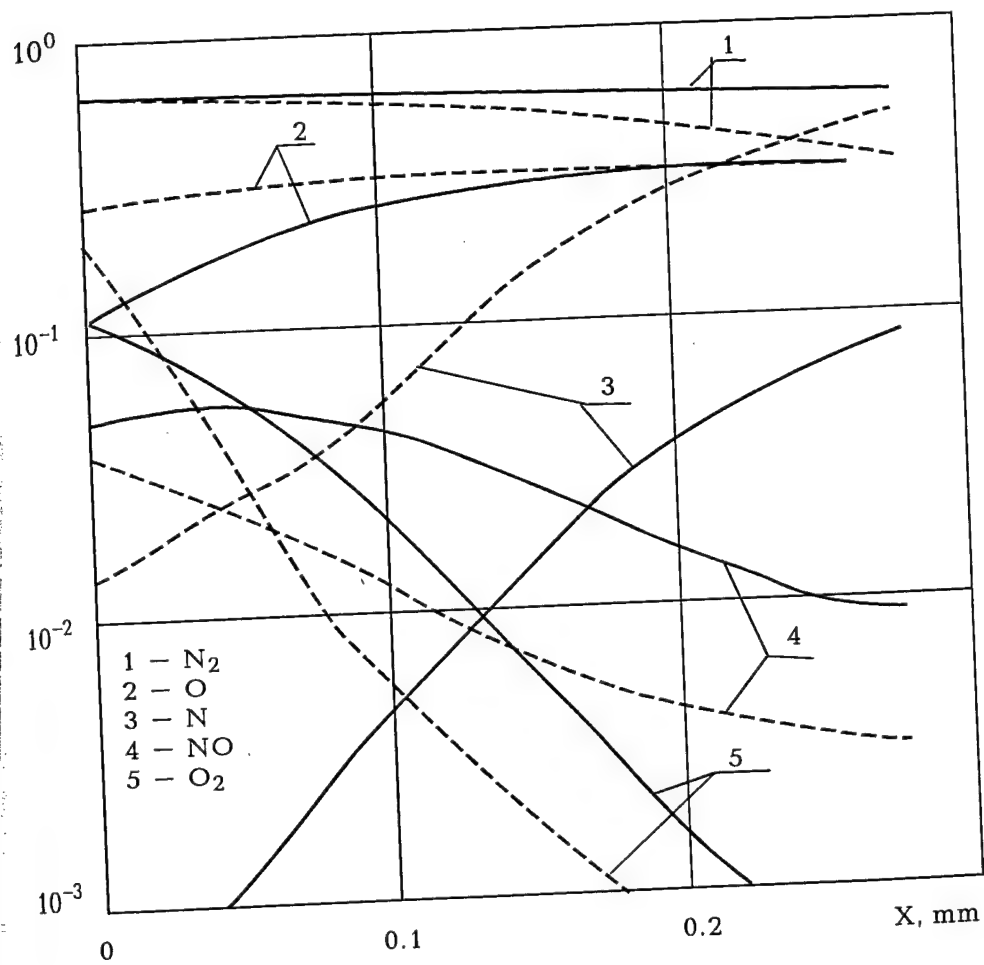


Fig. 12. Air component concentration distribution along the MHD - channel discharge zone for different thermodynamic flow models

----- equilibrium model  
 — nonequilibrium model

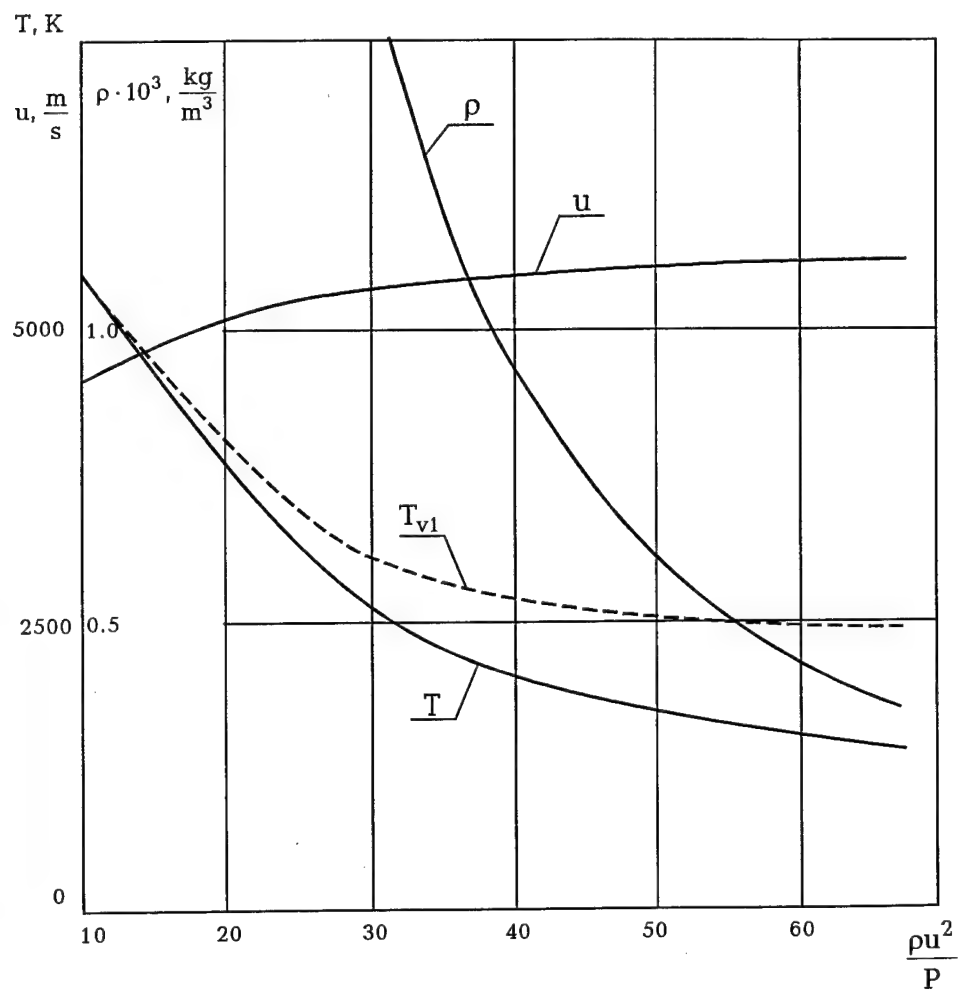


Fig.13. Parameter distribution along the secondary nozzle.



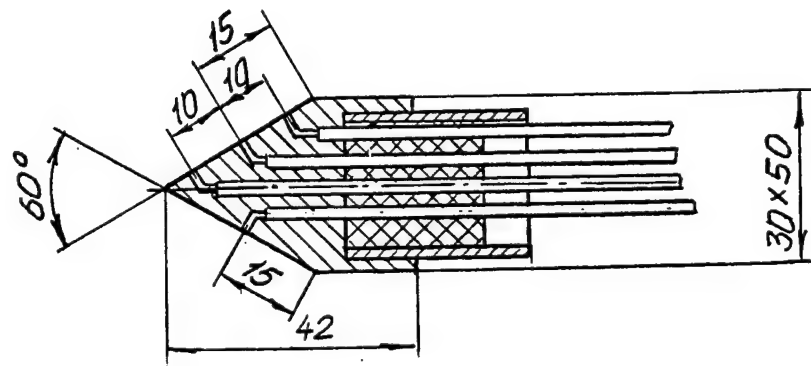
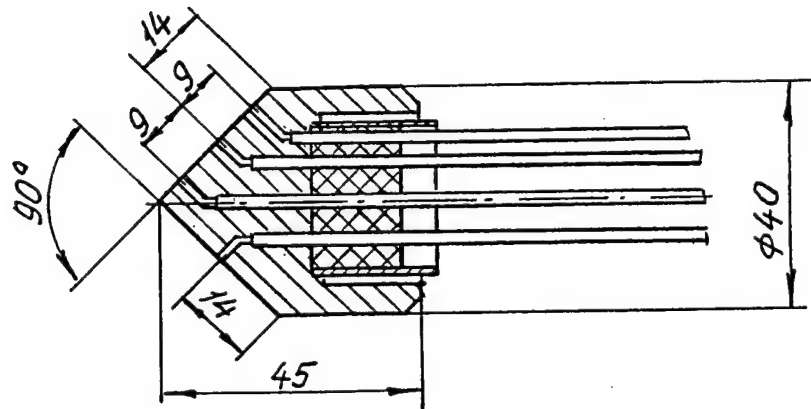
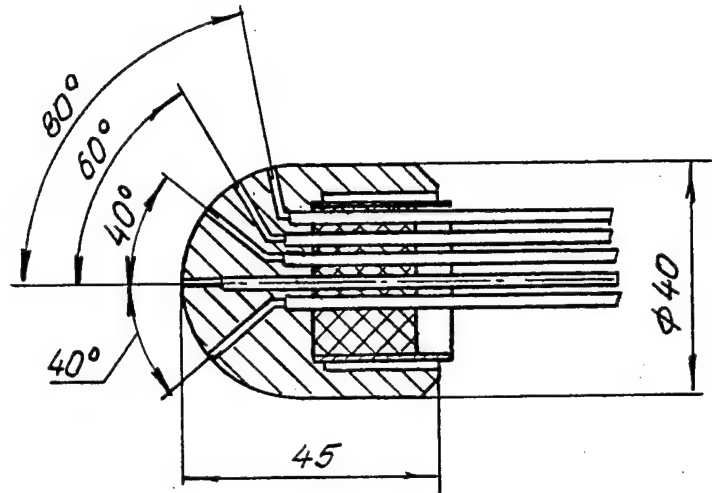


Fig.14. Model drawings



Fig. 15. Models without nickel coating.

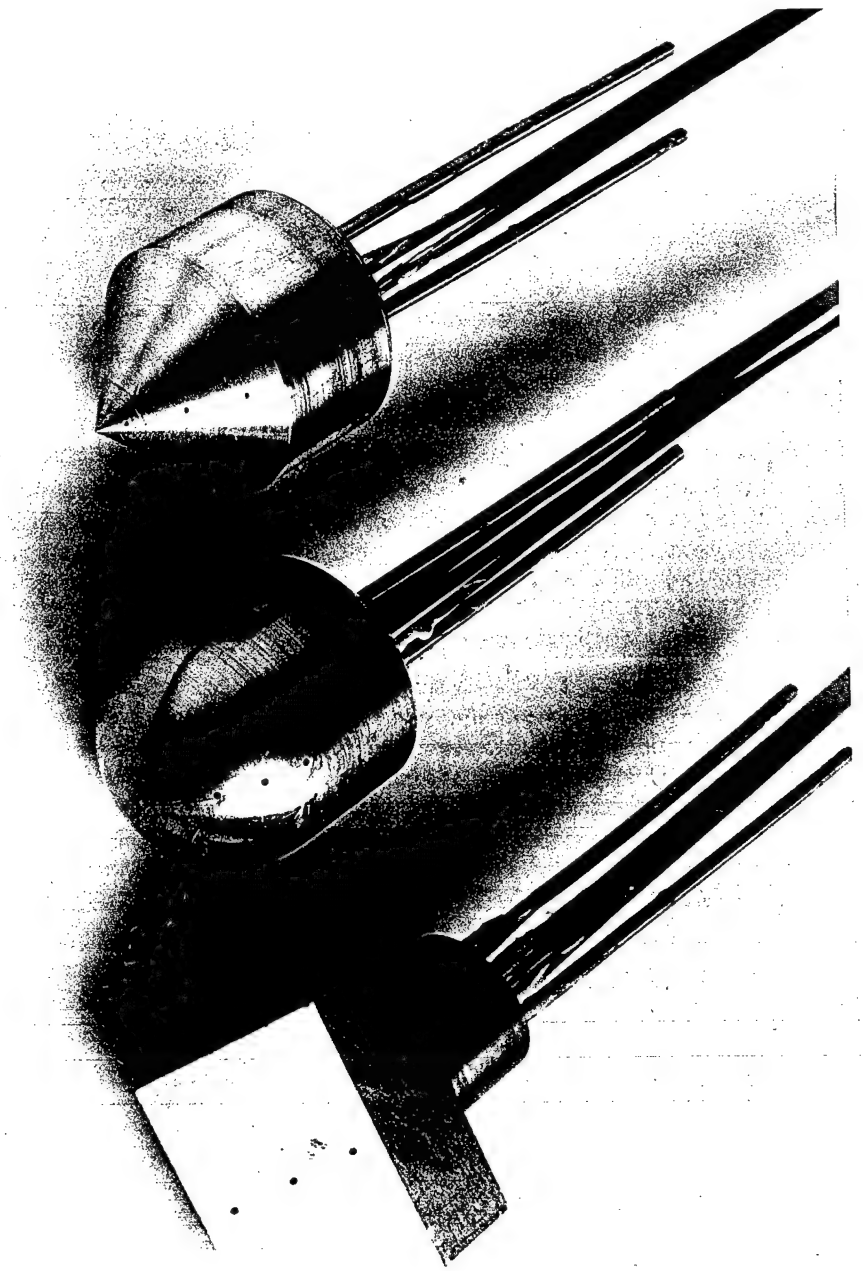


Fig. 16. Models covered with nickel.

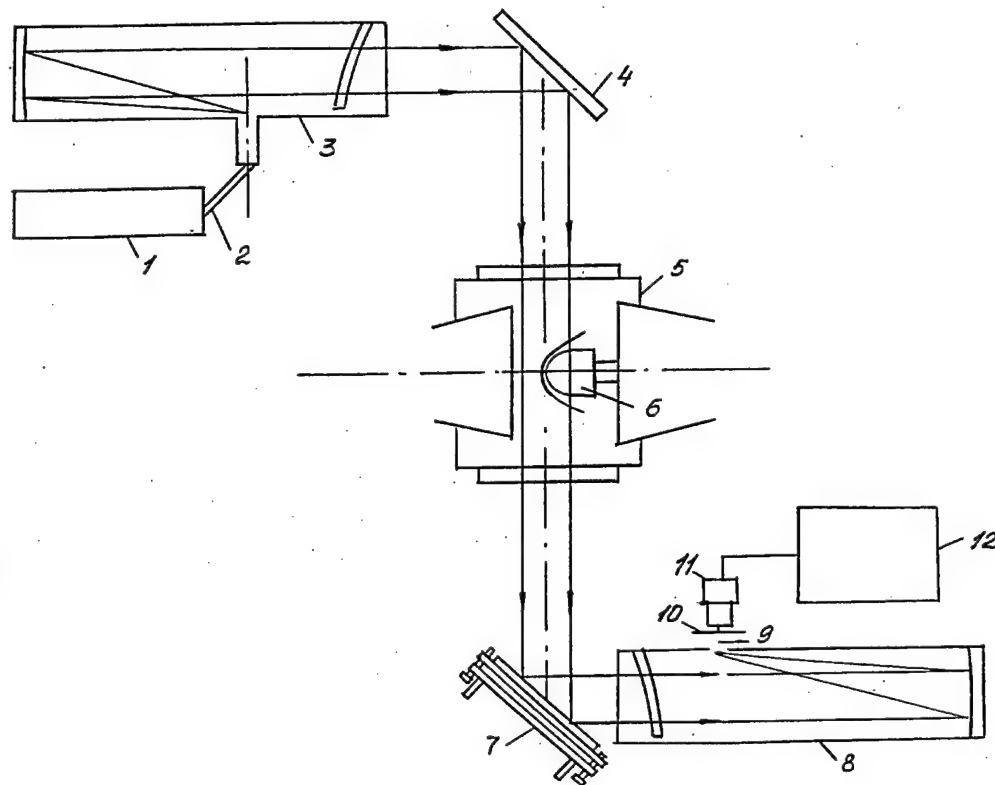


Fig.17. Schematic of a modernized shadow device

- 1 - Chromatic CMX - 4 laser;
- 2 - light guide;
- 3,8 - shadow device;
- 4 - rotational mirror;
- 5 - test section;
- 6 - test model;
- 7 - adjustable rotating mirror;
- 9 - Foucault knife;
- 10 - light filters;
- 11,12 - scientific - grade video camera and video tape

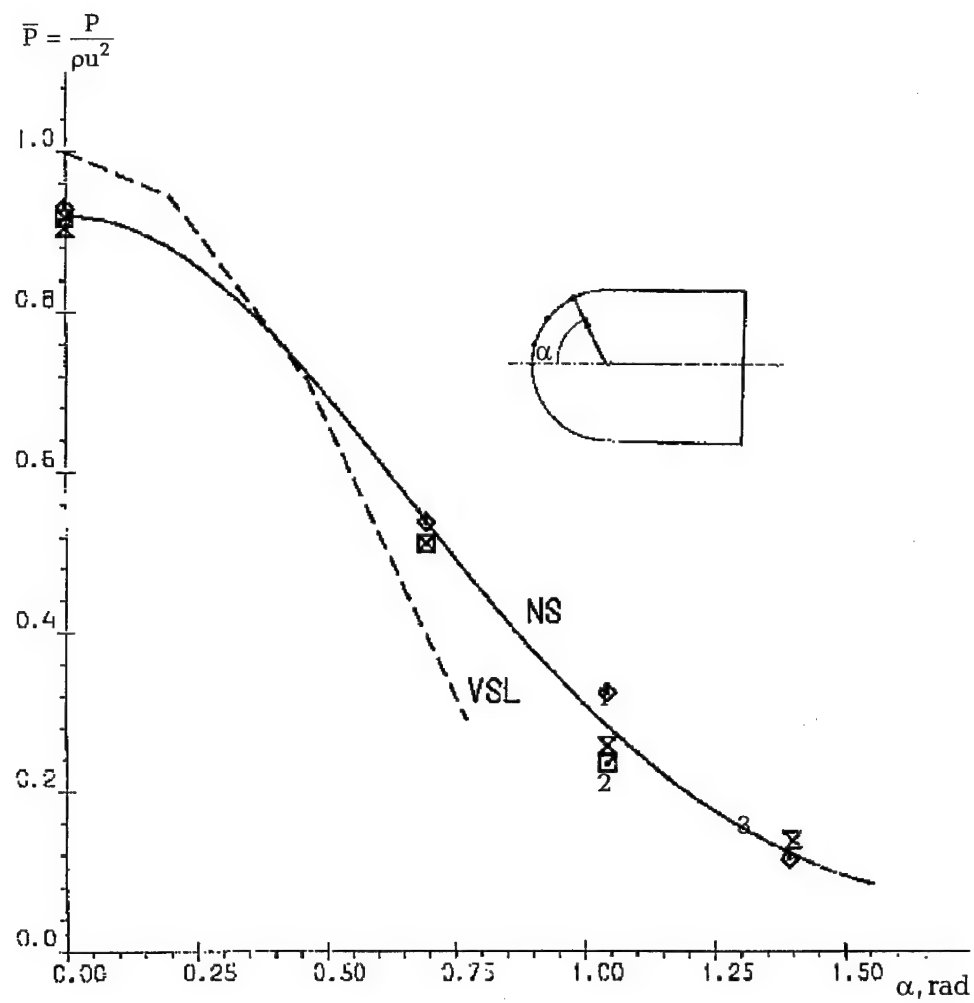


Fig.18. Pressure distributions over a hemisphere

1 - VAT-102; 2 - arc-heater; 3 - MHD-accelerator

----- VSL calculation

———— NS calculation

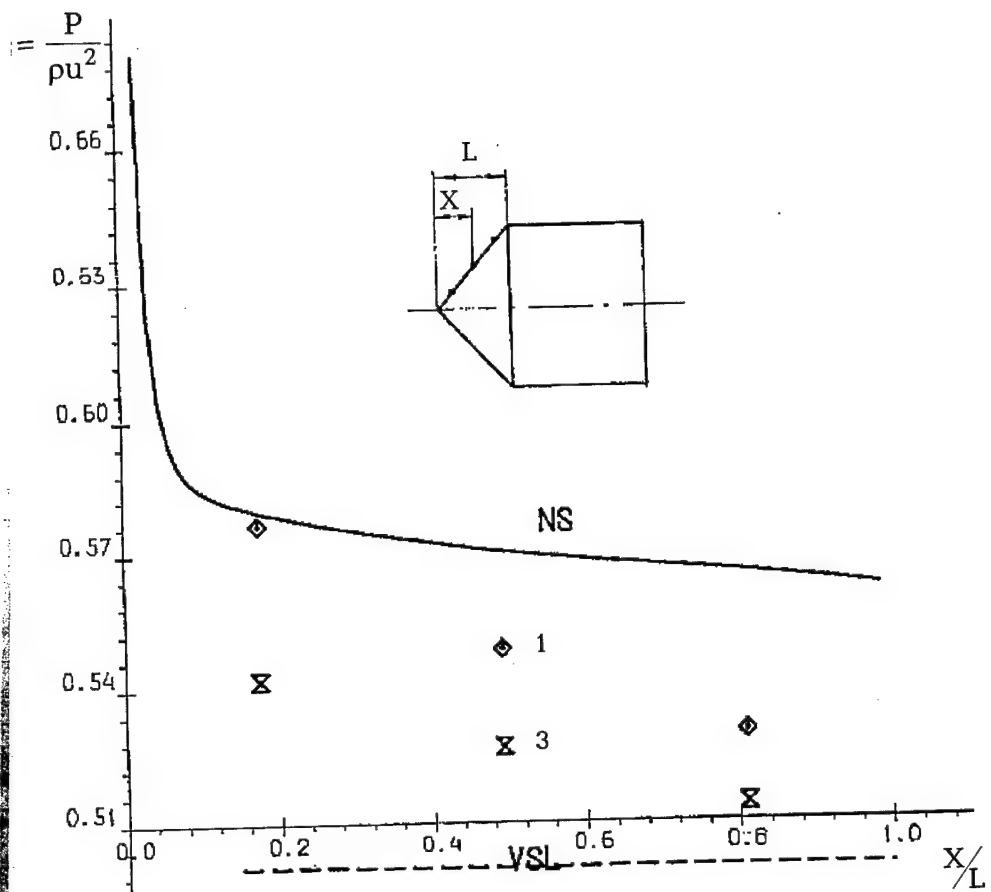


Fig.19. Pressure distributions over a cone

1 - VAT - 102; 3 - MHD - accelerator;

----- VSL calculation

———— NS calculation

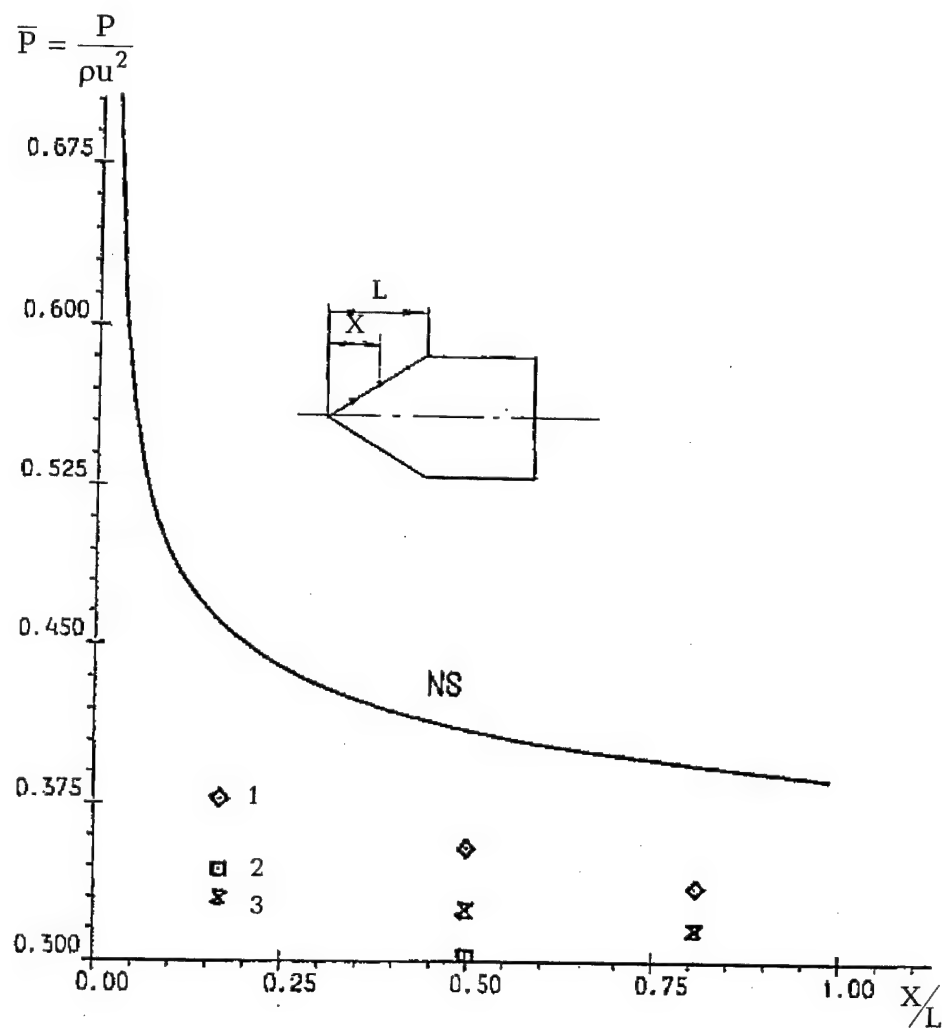


Fig.20. Pressure distributions over a wedge

1 - VAT - 102; 2 - arc - heater; 3 - MHD - accelerator;

— NS calculation

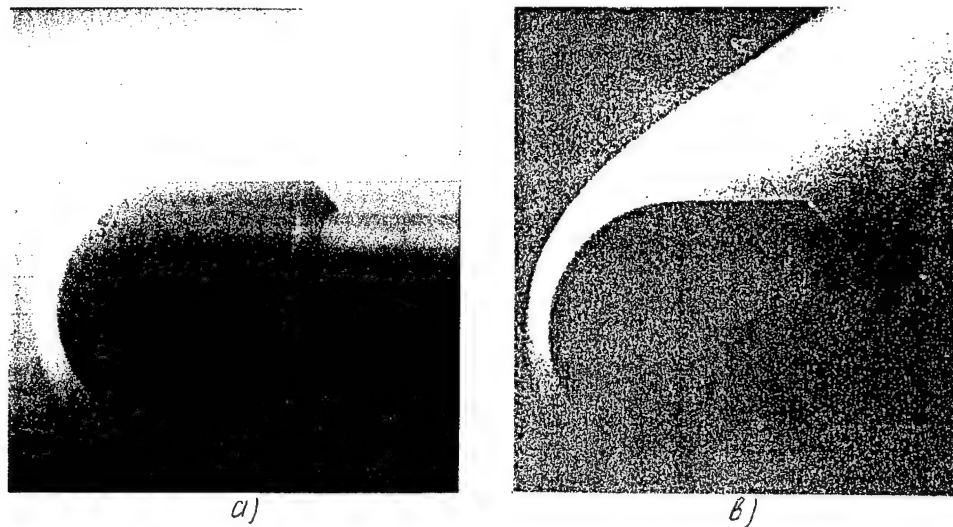


Fig. 21. Hypersonic wind tunnel VAT-102.  
 a) photo  
 b) video frame.

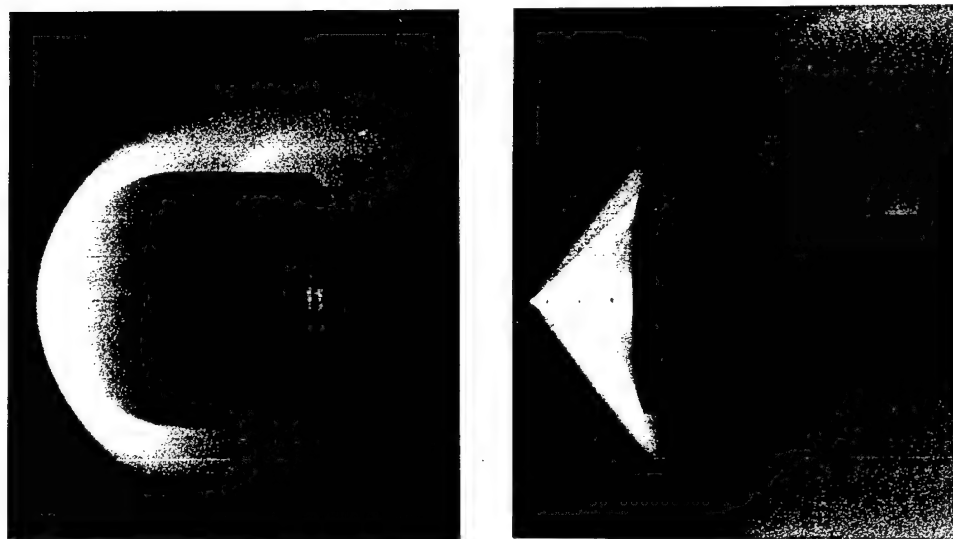
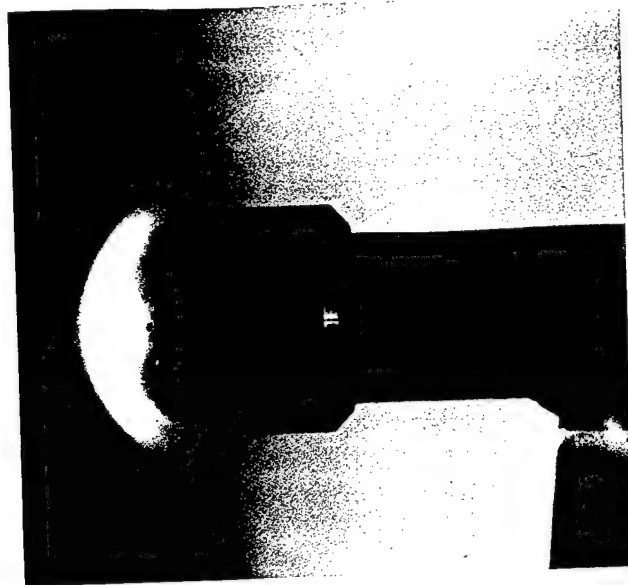
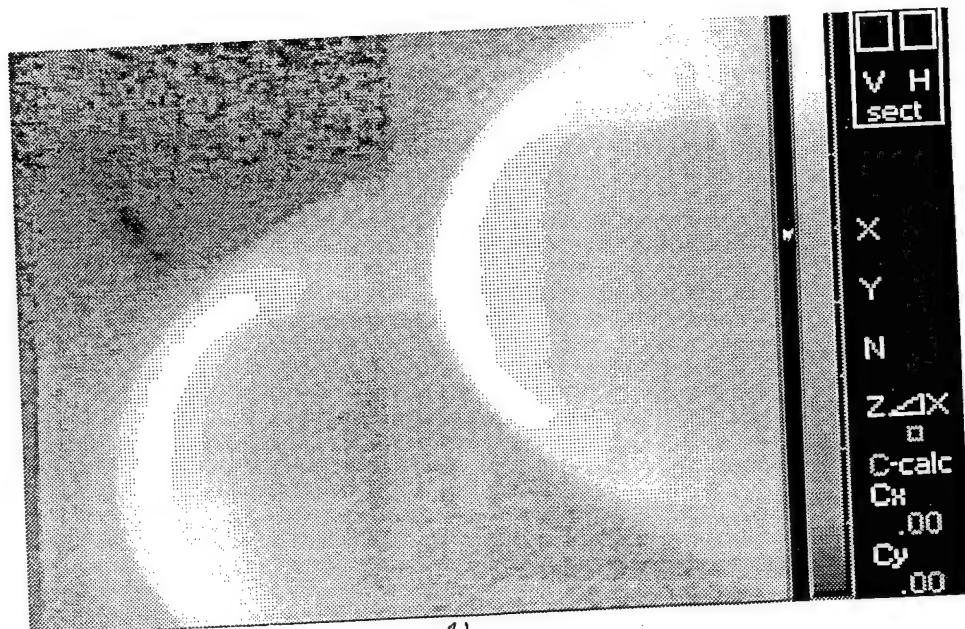


Fig. 22. Arc-heater. Flow pictures.





a)



b)

Fig. 23. MHD — accelerator.

a) photo

b) video frame



a)

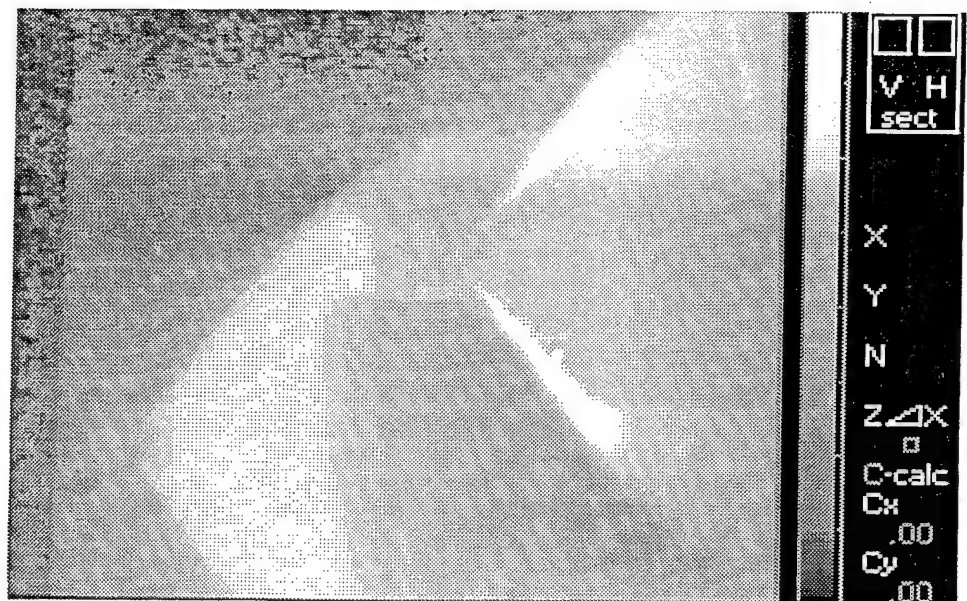
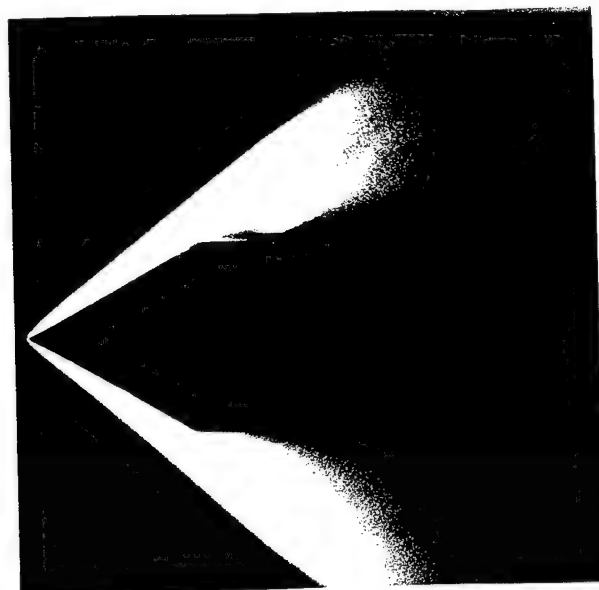


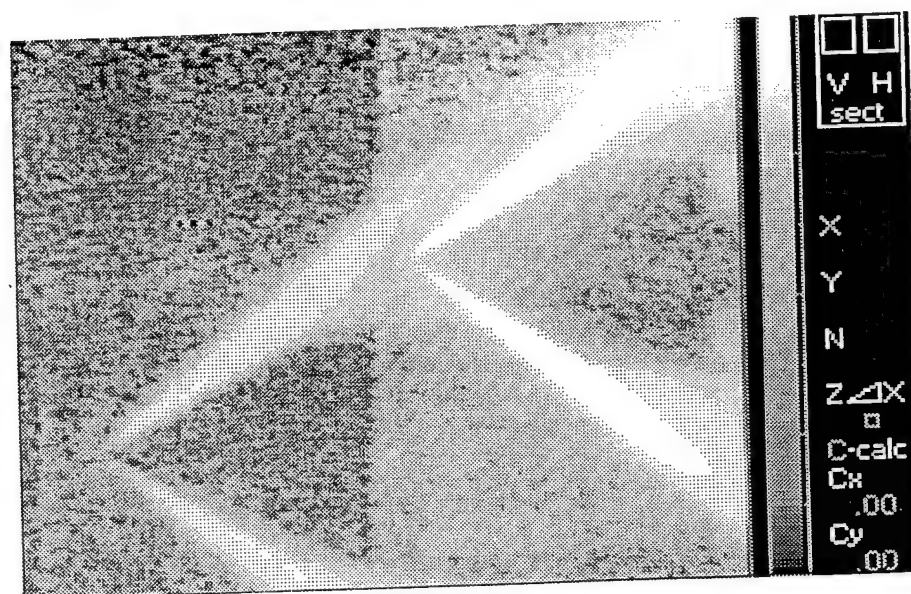
Fig. 24. MHD-accelerator (pictures on the left side are obtained by using an interference light filter and those on the right side by a neutral light filter)

a) photo

b) video frame



a)



b)

Fig. 25. MHD-accelerator (pictures on the left side are obtained by using an interference light filter and those on the right side by a neutral light filter)

a) photo

b) video frame

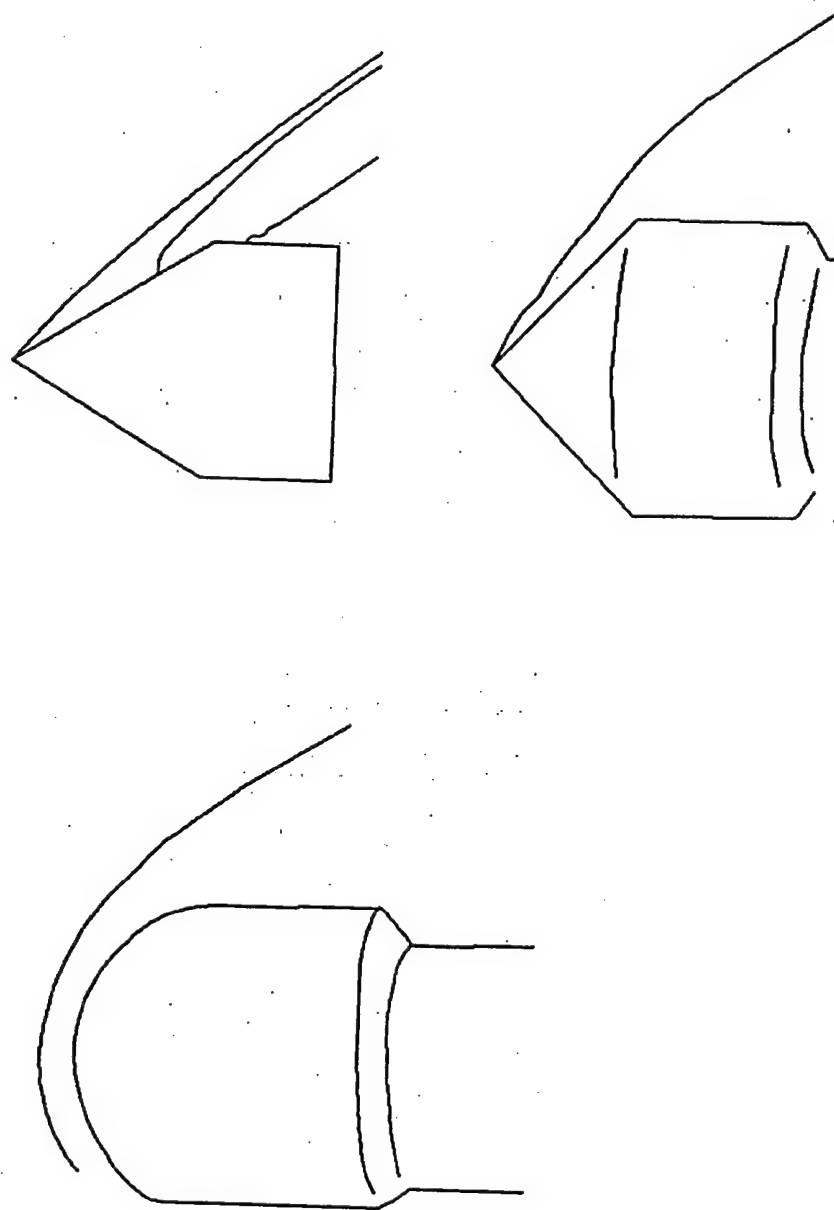


Fig.26. Examples of decoding video frames for the wind tunnel VAT-102

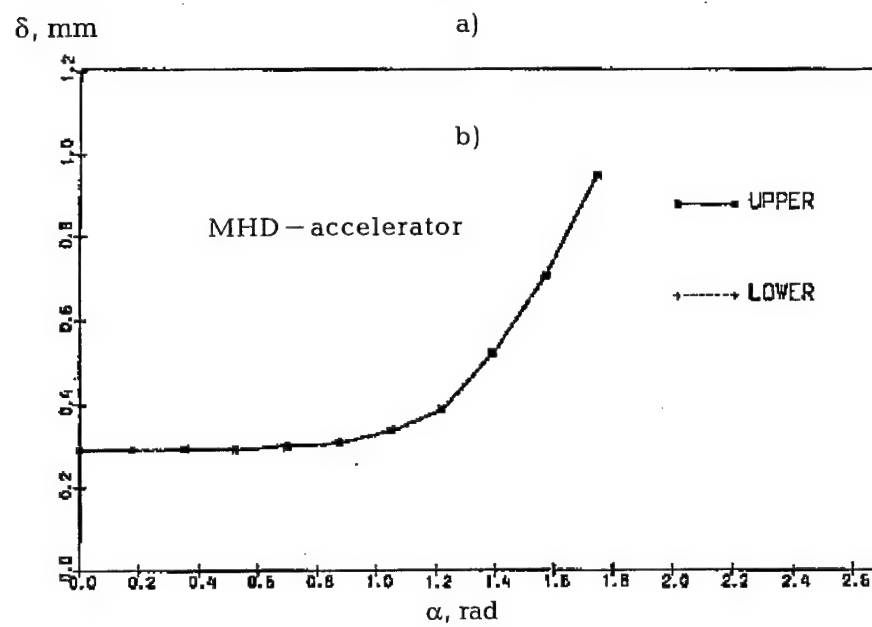
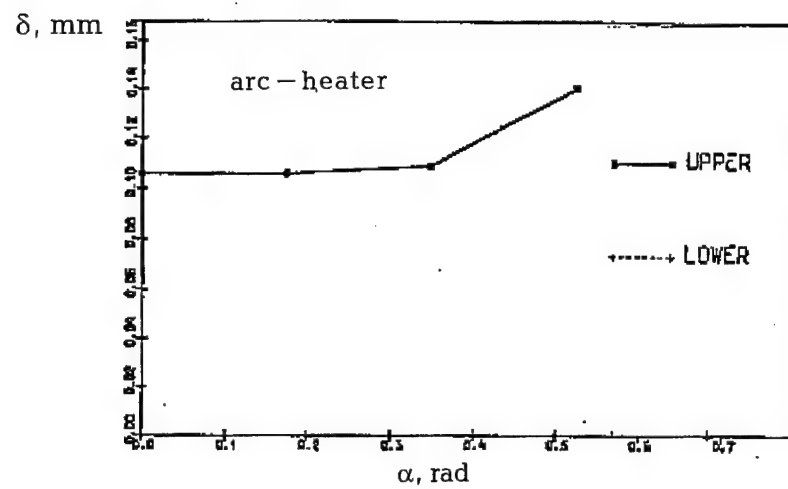
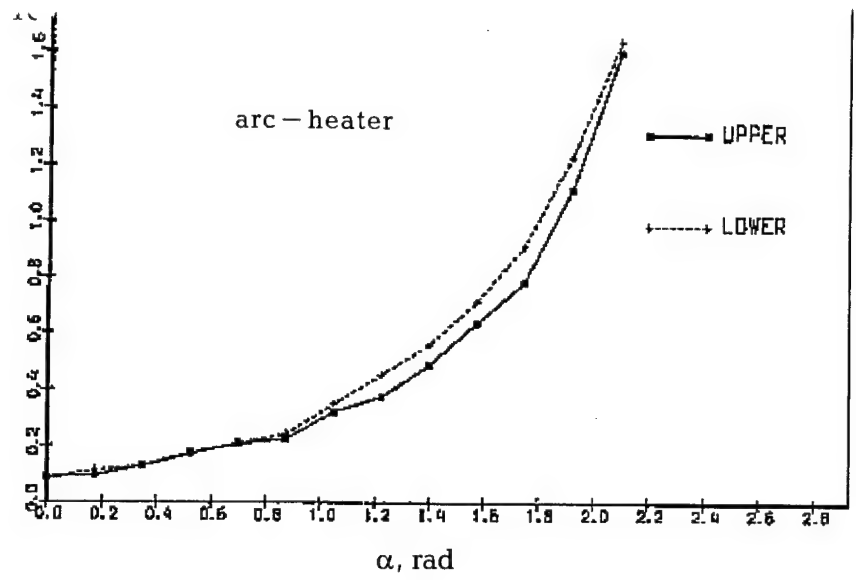


Fig.27. Flow glow zone stand-off distances for a hemisphere.



a)

b)

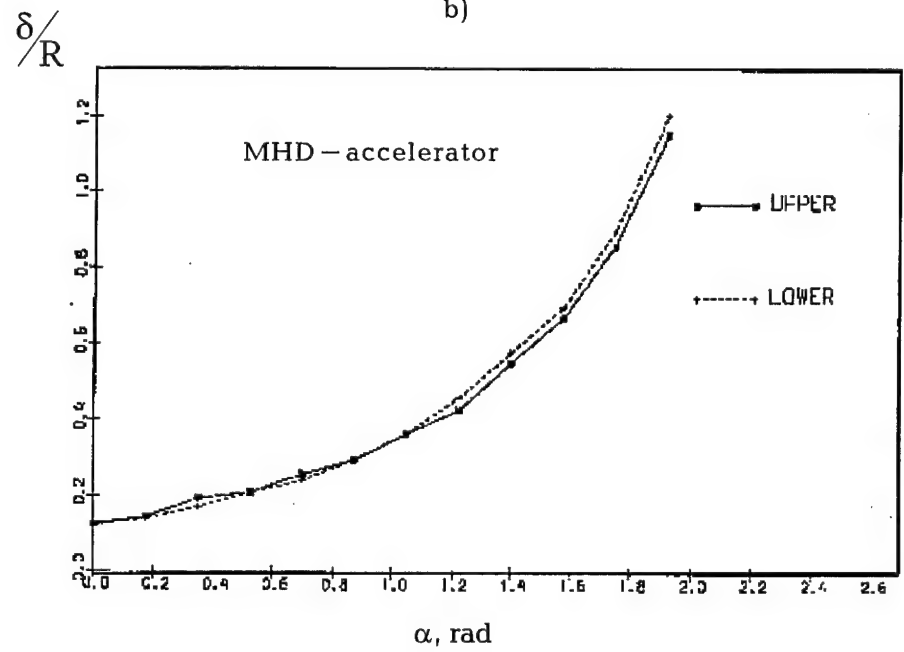


Fig.28. Shock wave stand - off distances for a hemisphere obtained from shadow pictures

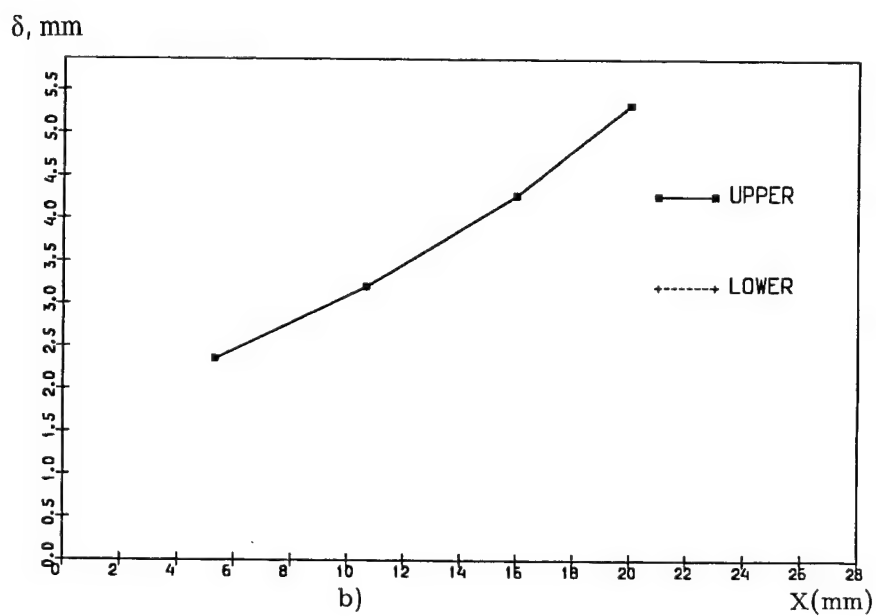
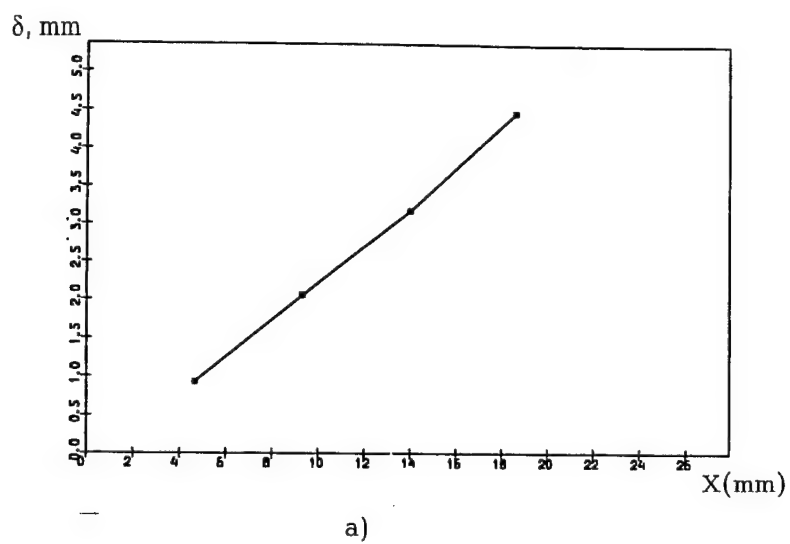


Fig.29. Flow glow zone stand-off distances (a) and shock wave stand-offs (shadow pictures) for a cone.

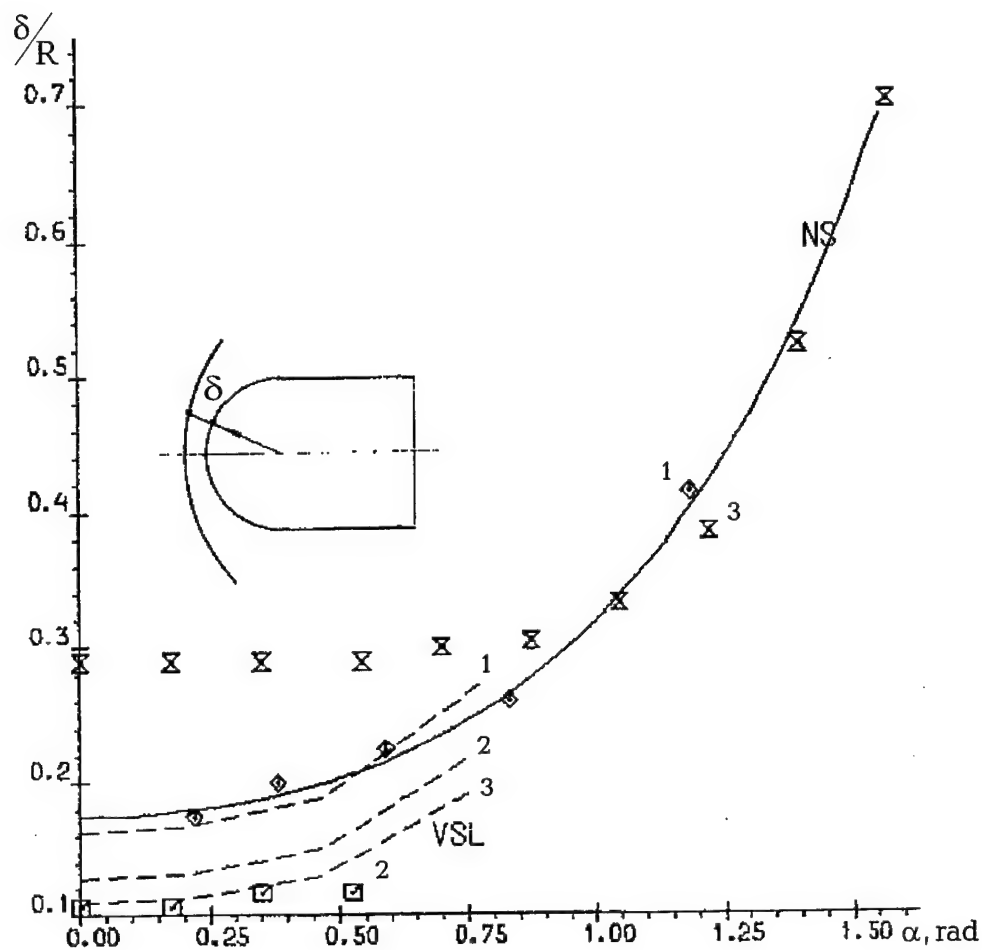


Fig.30. Flow glow zone stand-off distances for a hemisphere (test data are shown by points and calculated data by lines)  
 1 - VAT-102; 2 - arc-heater wind tunnel;  
 3 - MHD-acceleration wind tunnel



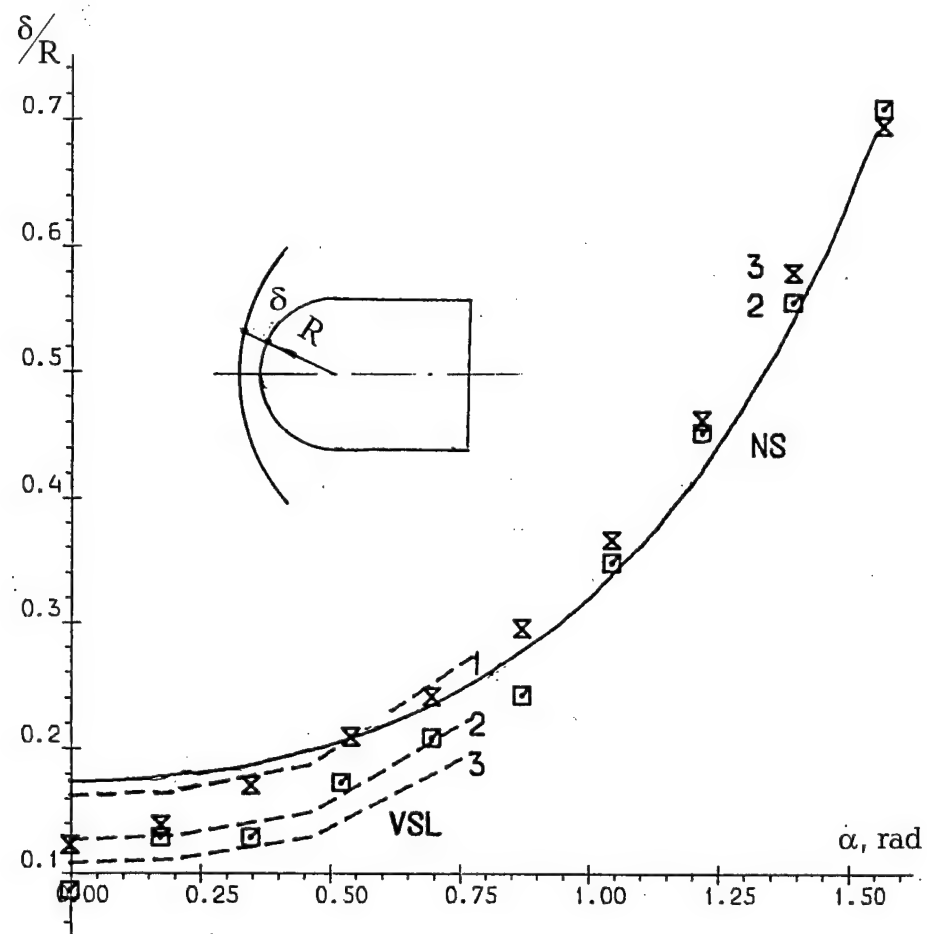


Fig. 31. Shock wave stand-off distances for a hemisphere obtained from shadow pictures (test data are shown by points and calculated data by lines)

1 - VAT-102; 2 - arc-heater wind tunnel;

3 - MHD-acceleration wind tunnel

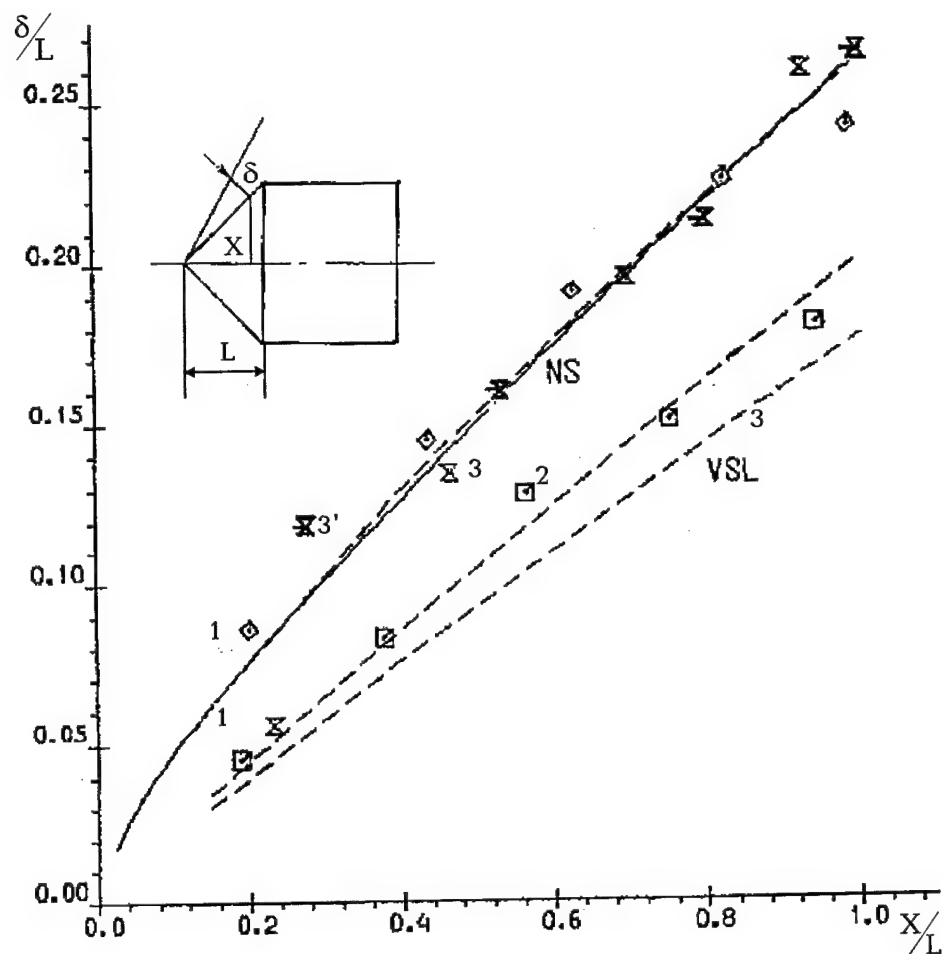


Fig.32. Flow glow zone stand-off distances and shock wave stand-offs (shadow picture) for a cone (test data are denoted by points and calculated data by lines)

1 - VAT-102; 2 - arc-heater;

3 - MHD-accelerator;

3' - MHD-accelerator (shadow picture)

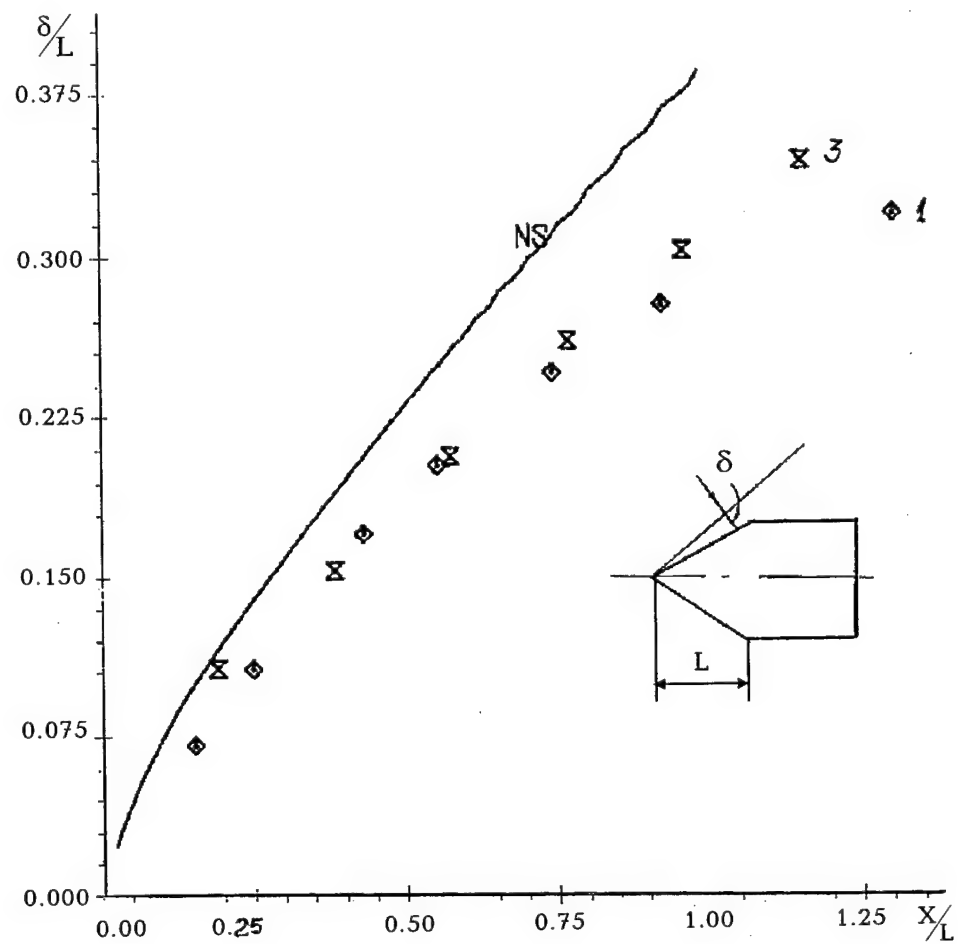


Fig.33. Flow glow zone stand-off distances for a wedge (test data are denoted by points and calculated data by lines)

1 - VAT-102; 3 - MHD-accelerator

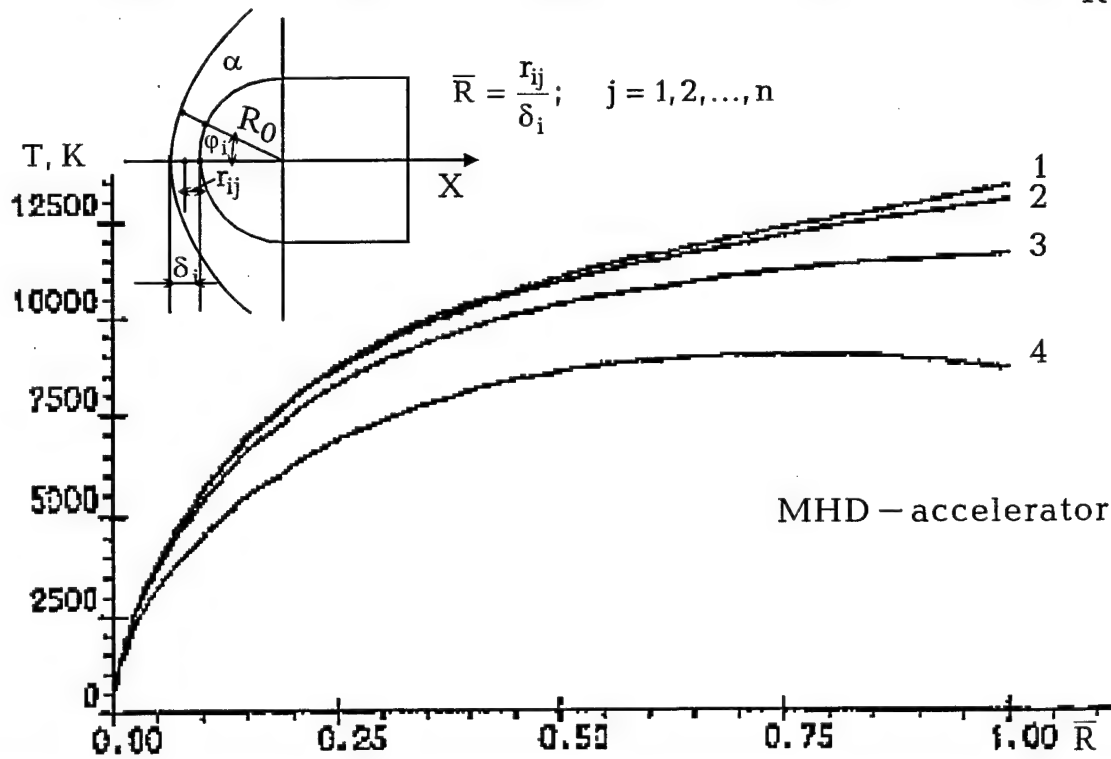
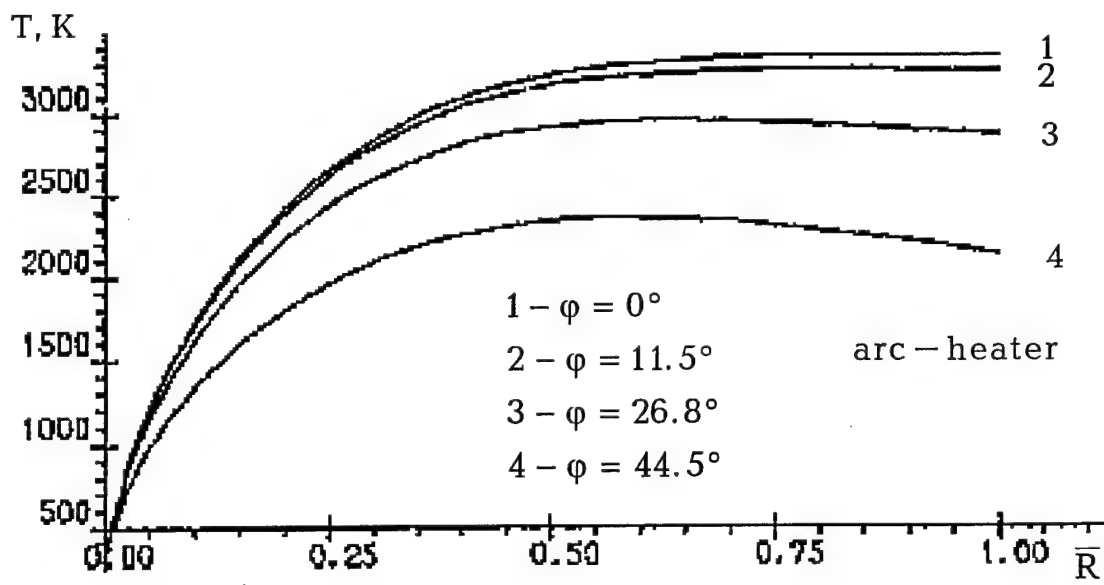
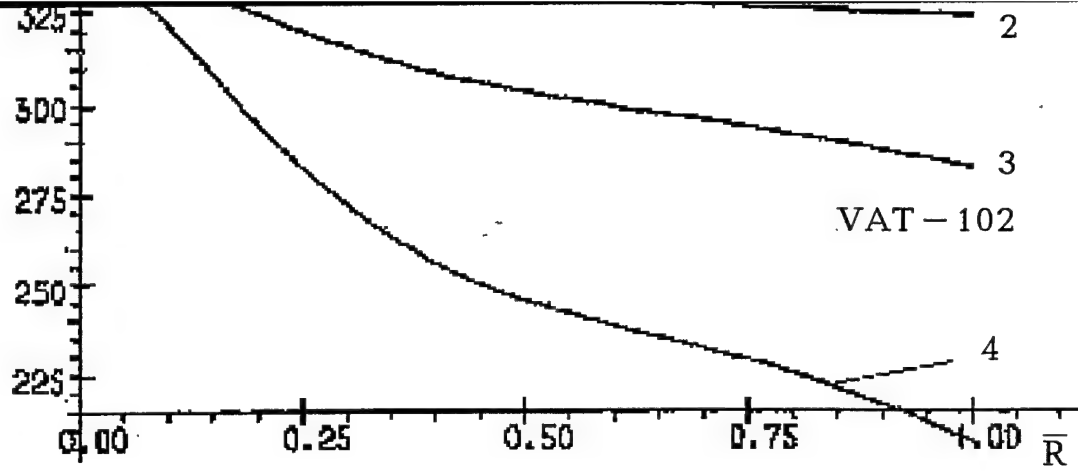


Fig.34. Temperature field in a shock layer near a hemisphere.

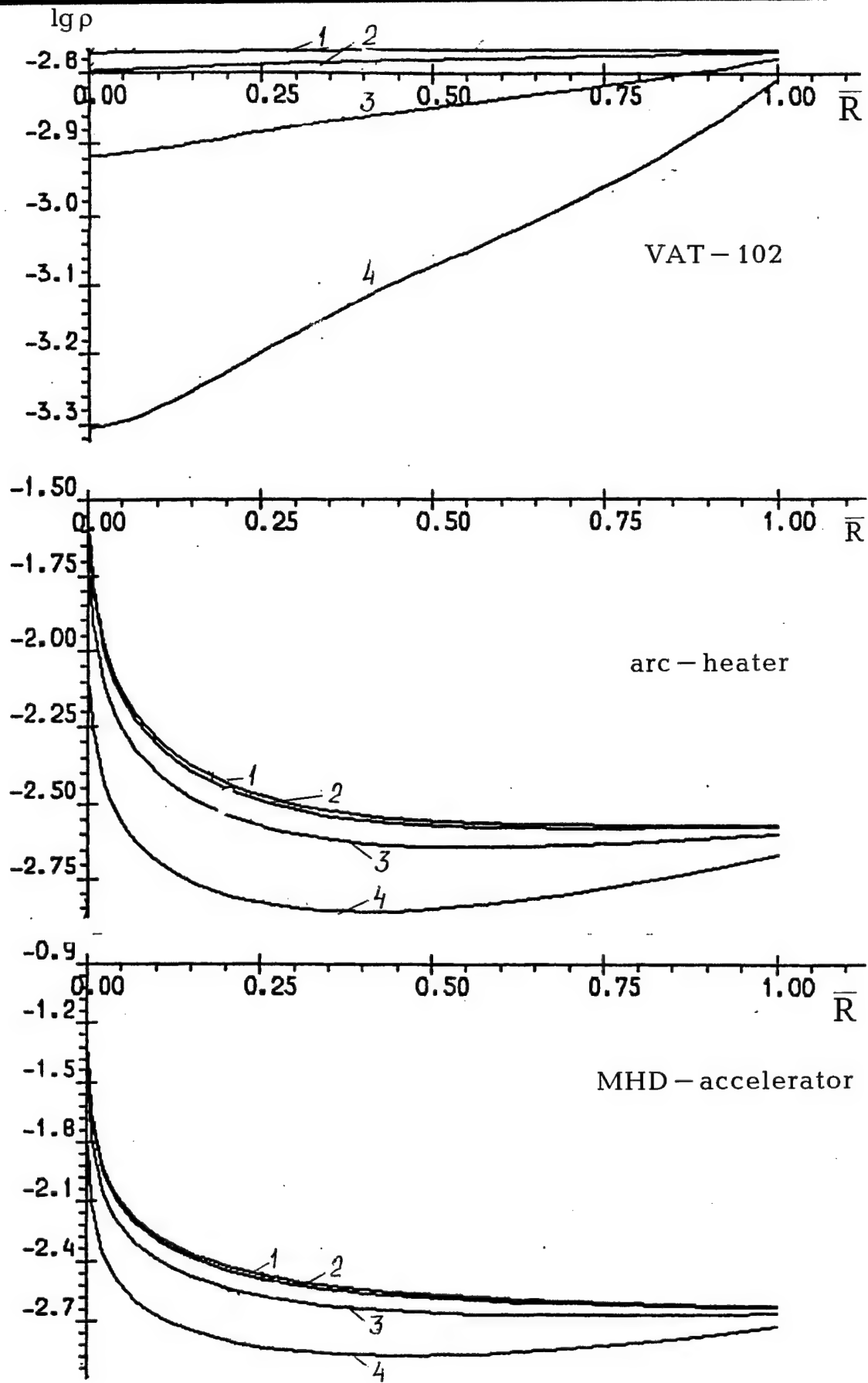


Fig.35. Density field in a shock layer near a hemisphere

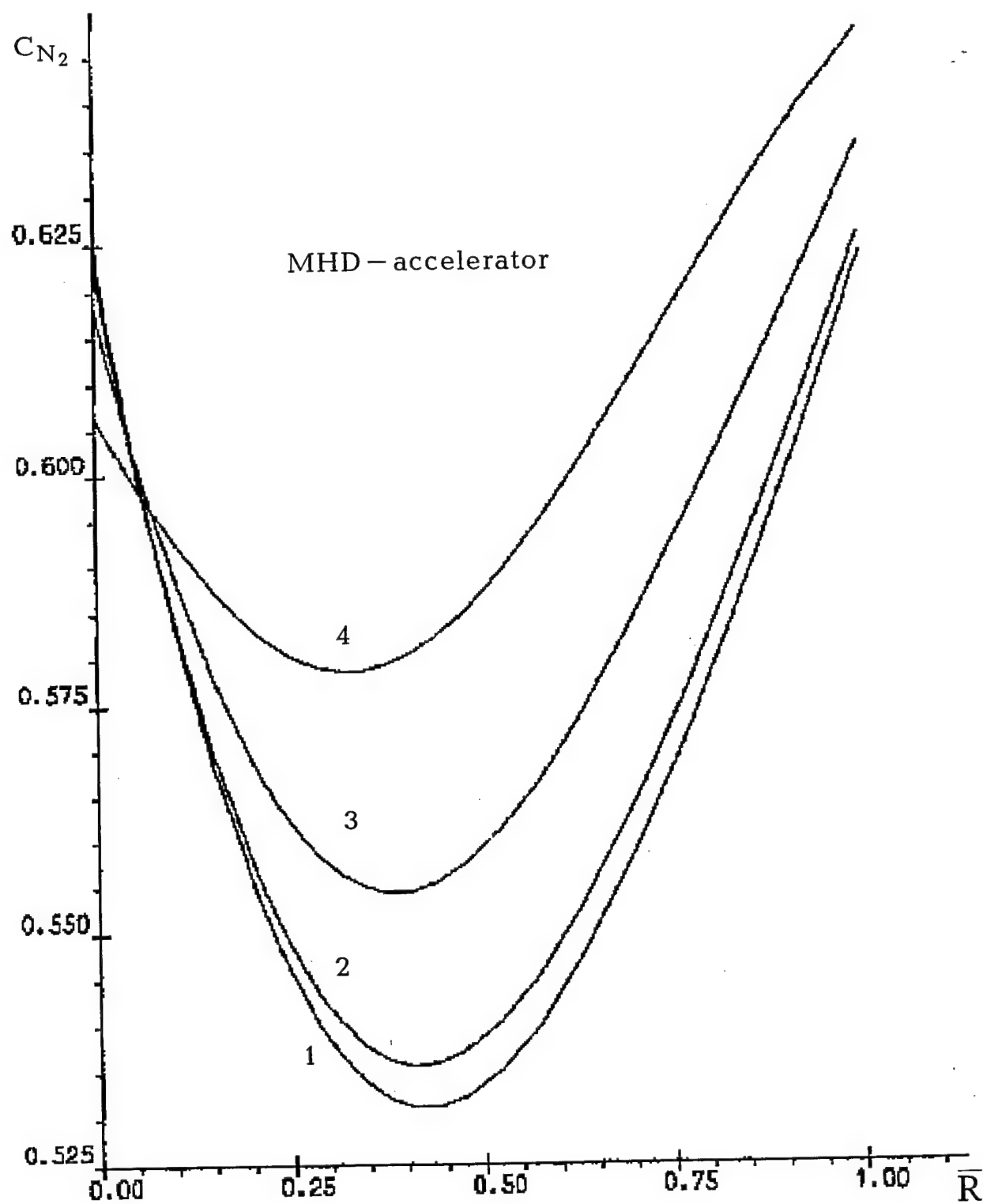


Fig.36.  $N_2$  concentration field in a shock layer near a hemisphere

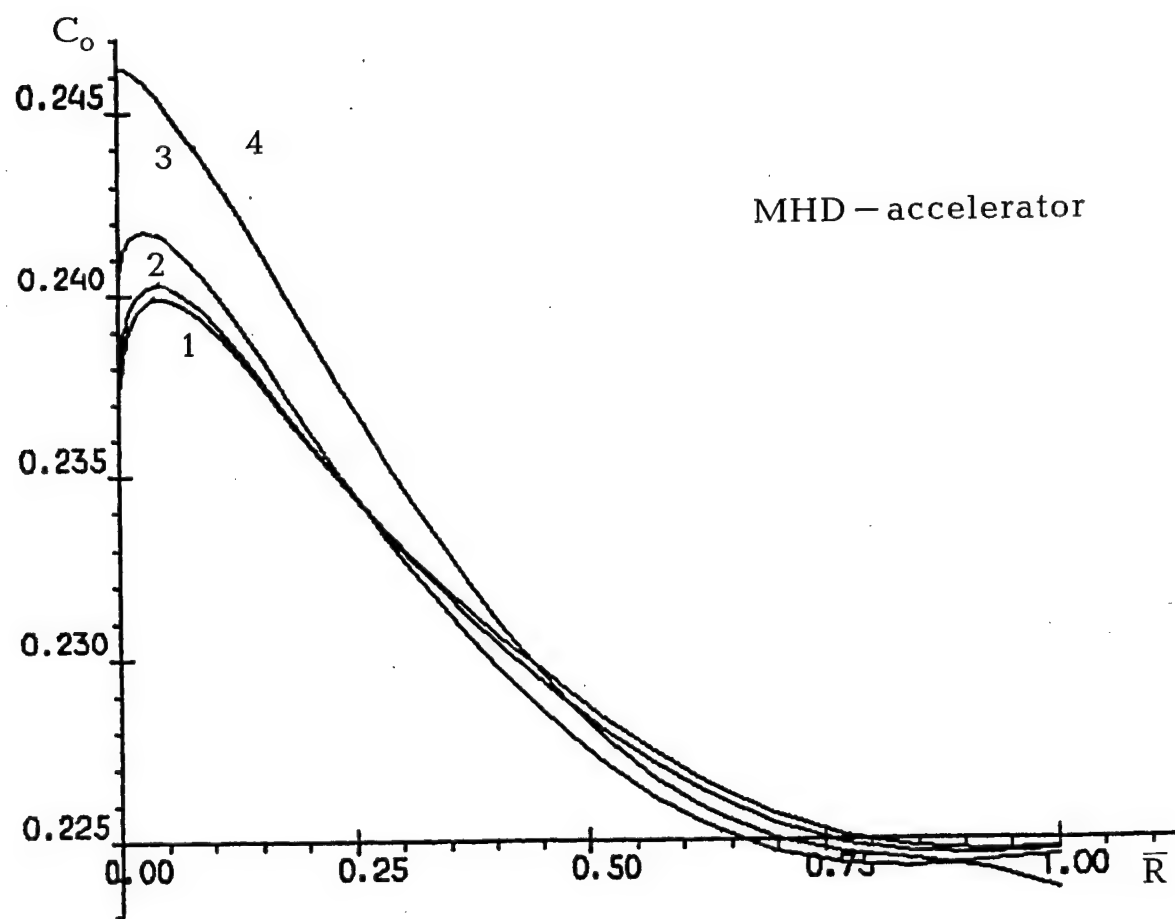
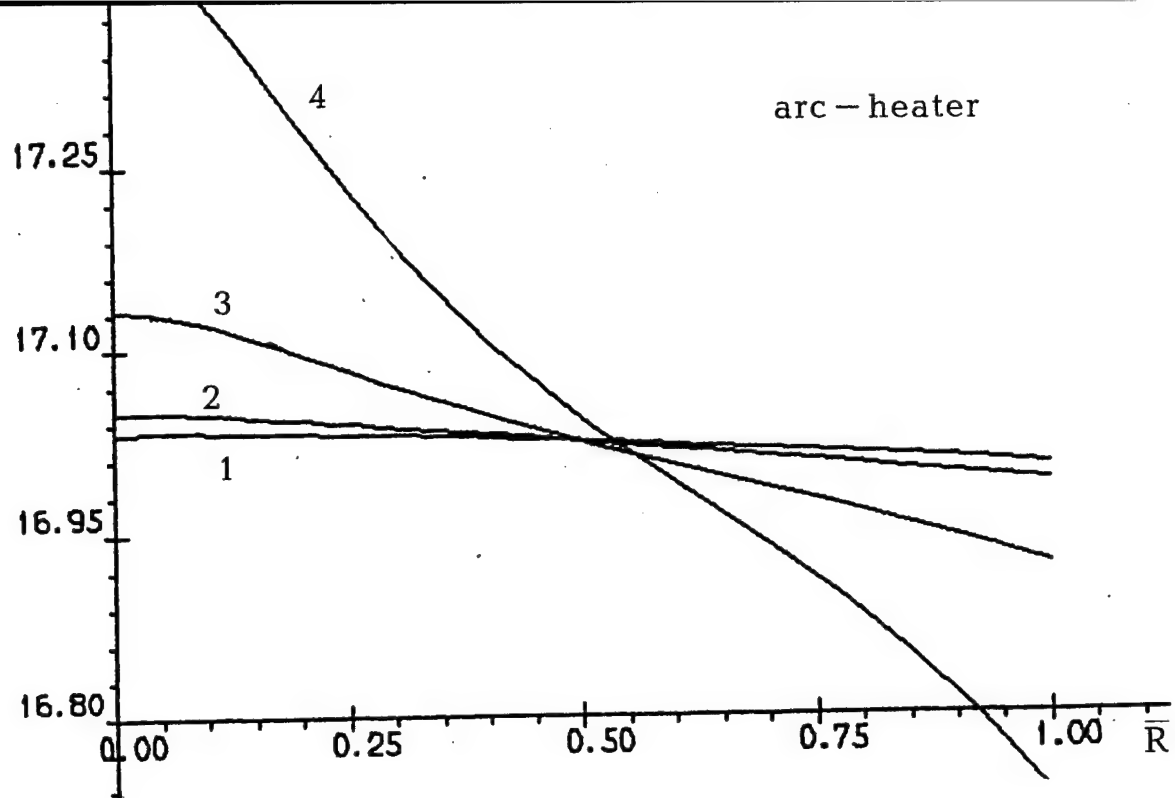


Fig. 37. O atom concentration field in a shock layer near a hemisphere.

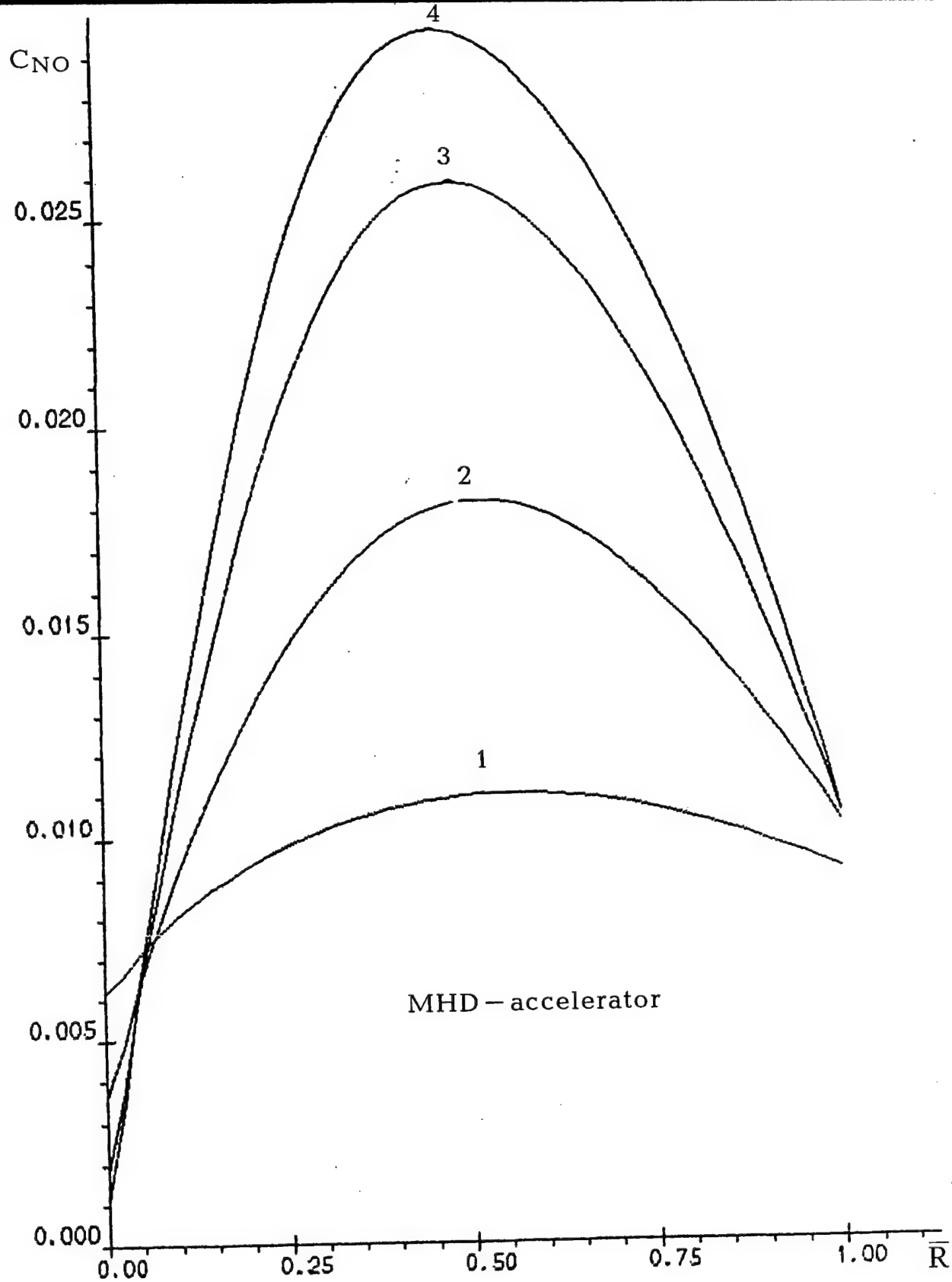


Fig.38. NO concentration field in a shock layer near a hemisphere.



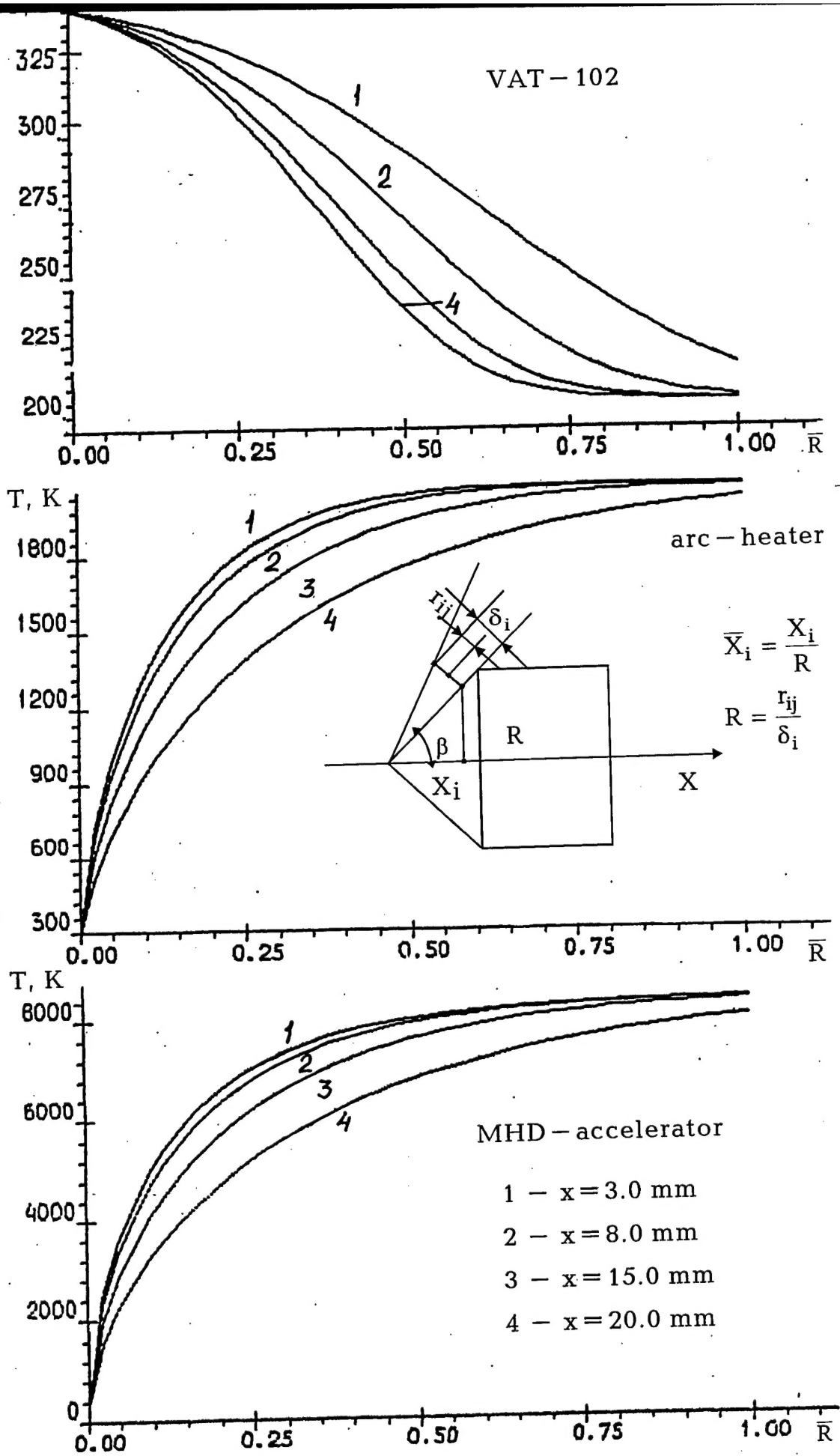


Fig.39. Temperature field in a shock layer near a cone.

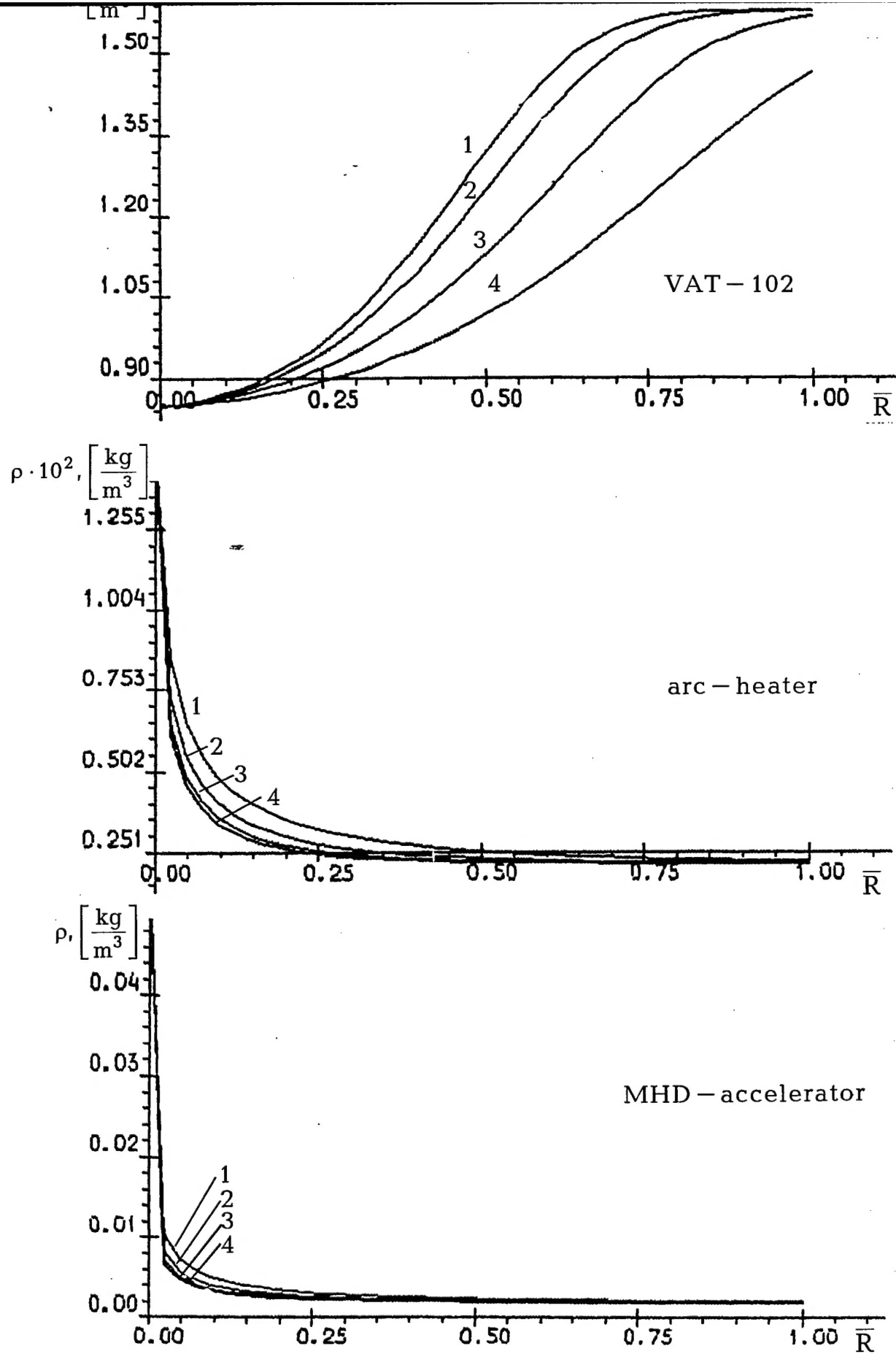


Fig.40. Density field in a shock layer near a cone.

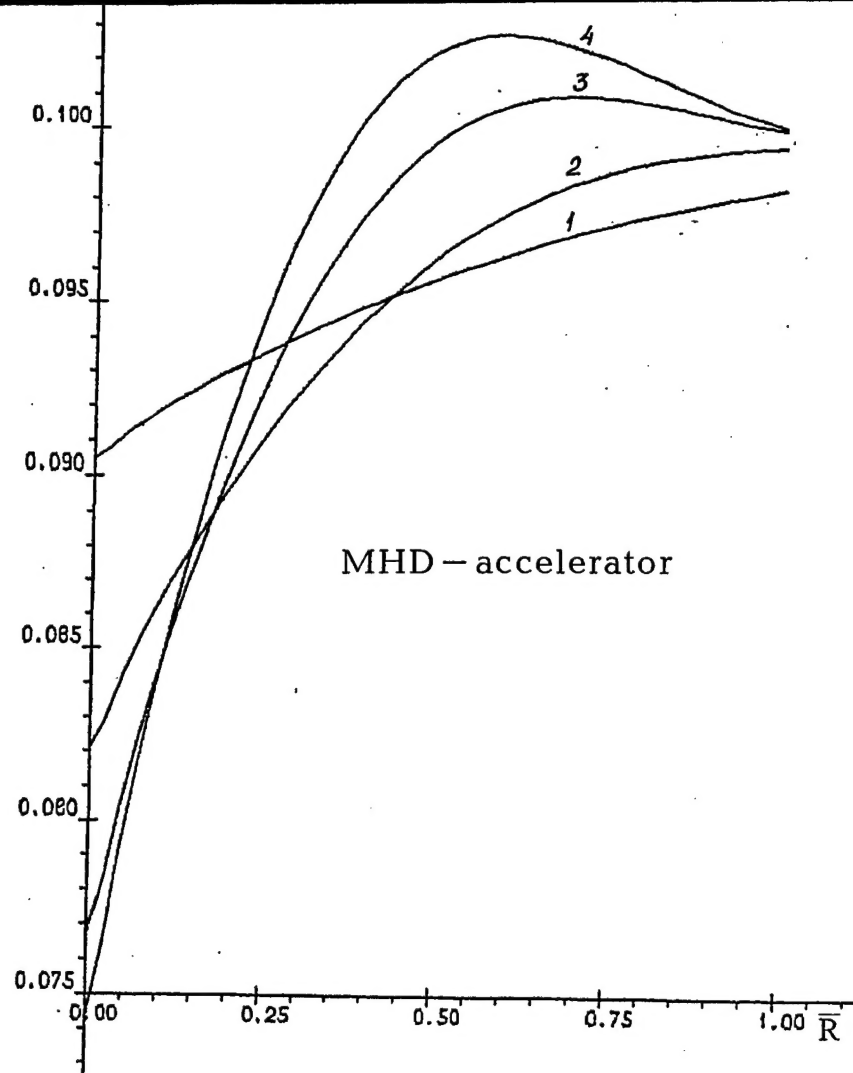


Fig.41. Nitrogen atom concentration field in a shock layer near a cone.

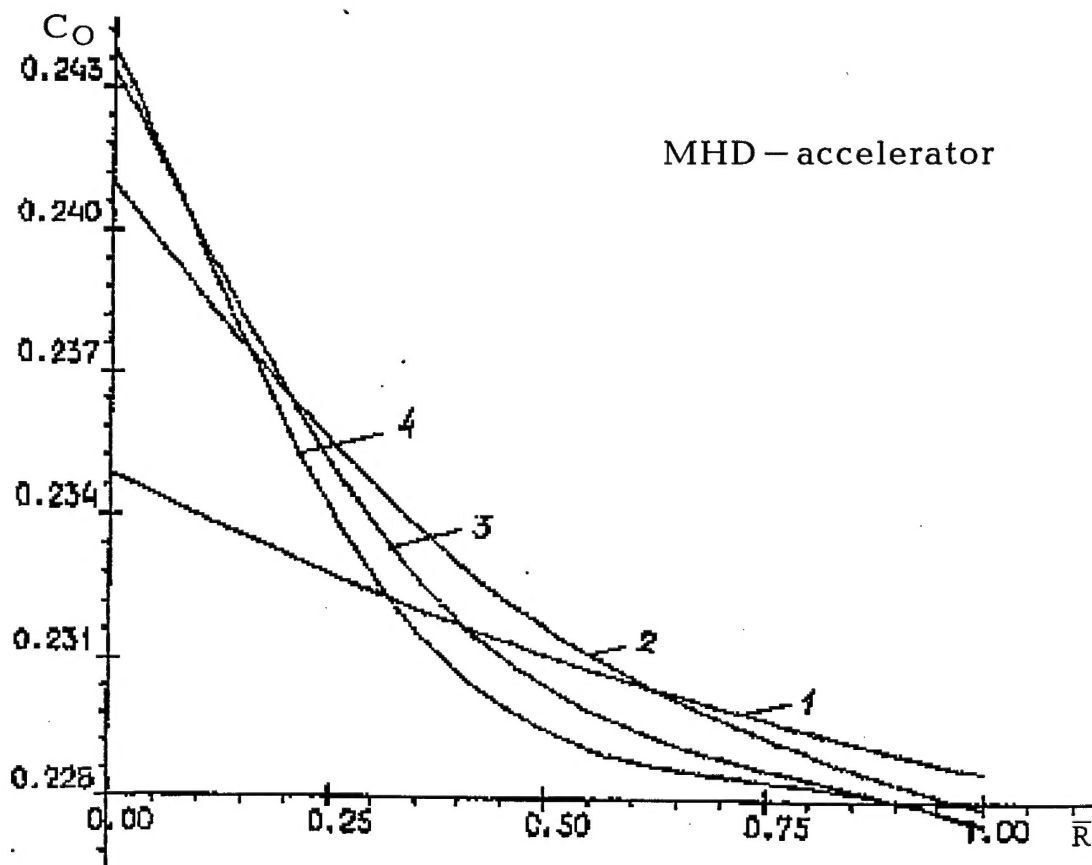


Fig.42. Oxygen atom concentration field in a shock layer near a cone.

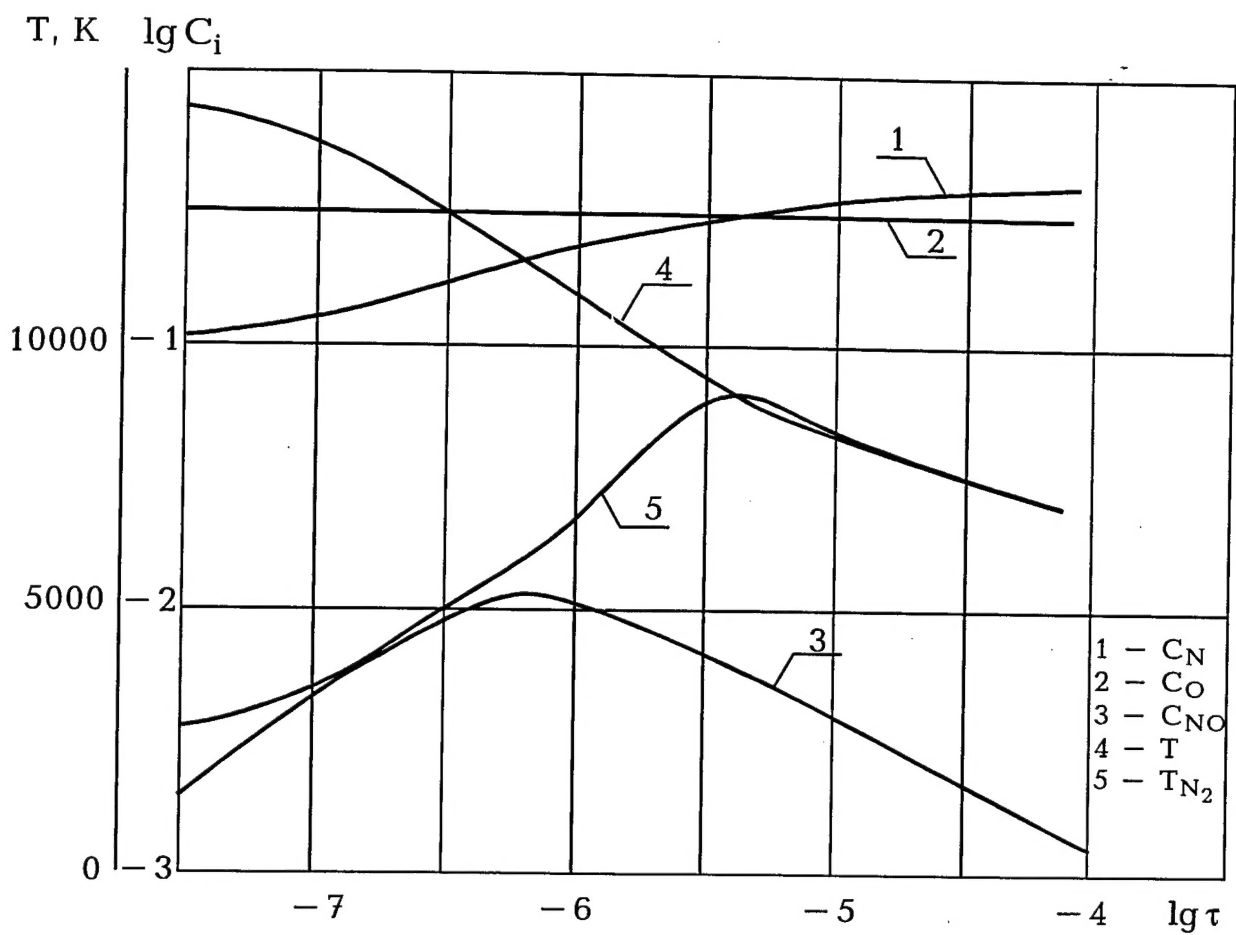


Fig.43. Variations of temperatures and concentrations of air components and air with Na and K seeds with time behind a normal shock wave.